

Measurement of inclusive jet cross sections in photoproduction at HERA

H1 Collaboration

Abstract

Inclusive jet cross sections are measured in photoproduction at HERA using the H1 detector. The data sample of $e^+p \rightarrow e^+ + jet + X$ events in the kinematic range of photon virtualities $Q^2 \leq 1 \text{ GeV}^2$ and photon-proton centre-of-mass energies $95 \leq W_{\gamma p} \leq 285 \text{ GeV}$ represents an integrated luminosity of 24.1 pb^{-1} . Jets are defined using the inclusive k_{\perp} algorithm. Single- and multi-differential cross sections are measured as functions of jet transverse energy E_T^{jet} and pseudorapidity η^{jet} in the domain $5 \leq E_T^{jet} \leq 75 \text{ GeV}$ and $-1 \leq \eta^{jet} \leq 2.5$. The cross sections are found to be in good agreement with next-to-leading order perturbative QCD calculations corrected for fragmentation and underlying event effects. The cross section differential in E_T^{jet} , which varies by six orders of magnitude over the measured range, is compared with similar distributions from $p\bar{p}$ colliders at equal and higher energies.

Submitted to Eur. Phys. J. C

C. Adloff³³, V. Andreev²⁴, B. Andrieu²⁸, T. Anthonis⁴, A. Astvatsatourov³⁵, A. Babaev²³,
 J. Bähr³⁵, P. Baranov²⁴, E. Barrelet²⁸, W. Bartel¹⁰, S. Baumgartner³⁶, J. Becker³⁷,
 M. Beckingham²¹, A. Beglarian³⁴, O. Behnke¹³, A. Belousov²⁴, Ch. Berger¹, T. Berndt¹⁴,
 J.C. Bizot²⁶, J. Böhme¹⁰, V. Boudry²⁷, W. Braunschweig¹, V. Brisson²⁶, H.-B. Bröker²,
 D.P. Brown¹⁰, D. Bruncko¹⁶, F.W. Büsler¹¹, A. Bunyatyan^{12,34}, A. Burrage¹⁸, G. Buschhorn²⁵,
 L. Bystritskaya²³, A.J. Campbell¹⁰, S. Caron¹, F. Cassol-Brunner²², V. Chekelian²⁵,
 D. Clarke⁵, C. Collard⁴, J.G. Contreras^{7,41}, Y.R. Coppens³, J.A. Coughlan⁵, M.-C. Cousinou²²,
 B.E. Cox²¹, G. Cozzika⁹, J. Cvach²⁹, J.B. Dainton¹⁸, W.D. Dau¹⁵, K. Daum^{33,39},
 M. Davidsson²⁰, B. Delcourt²⁶, N. Delerue²², R. Demirchyan³⁴, A. De Roeck^{10,43},
 E.A. De Wolf⁴, C. Diaconu²², J. Dingfelder¹³, P. Dixon¹⁹, V. Dodonov¹², J.D. Dowell³,
 A. Dubak²⁵, C. Duprel², G. Eckerlin¹⁰, D. Eckstein³⁵, V. Efremenko²³, S. Egli³², R. Eichler³²,
 F. Eisele¹³, E. Eisenhandler¹⁹, M. Ellerbrock¹³, E. Elsen¹⁰, M. Erdmann^{10,40,e}, W. Erdmann³⁶,
 P.J.W. Faulkner³, L. Favart⁴, A. Fedotov²³, R. Felst¹⁰, J. Ferencei¹⁰, S. Ferron²⁷,
 M. Fleischer¹⁰, P. Fleischmann¹⁰, Y.H. Fleming³, G. Flucke¹⁰, G. Flügge², A. Fomenko²⁴,
 I. Foresti³⁷, J. Formánek³⁰, G. Franke¹⁰, G. Frising¹, E. Gabathuler¹⁸, K. Gabathuler³²,
 J. Garvey³, J. Gassner³², J. Gayler¹⁰, R. Gerhards¹⁰, C. Gerlich¹³, S. Ghazaryan^{4,34},
 L. Goerlich⁶, N. Gogitidze²⁴, C. Grab³⁶, V. Grabski³⁴, H. Grässler², T. Greenshaw¹⁸,
 G. Grindhammer²⁵, D. Haidt¹⁰, L. Hajduk⁶, J. Haller¹³, B. Heinemann¹⁸, G. Heinzelmann¹¹,
 R.C.W. Henderson¹⁷, S. Hengstmann³⁷, H. Henschel³⁵, O. Henshaw³, R. Heremans⁴,
 G. Herrera^{7,44}, I. Herynek²⁹, M. Hildebrandt³⁷, M. Hilgers³⁶, K.H. Hiller³⁵, J. Hladký²⁹,
 P. Höting², D. Hoffmann²², R. Horisberger³², A. Hovhannisyan³⁴, M. Ibbotson²¹, Ç. İşsever⁷,
 M. Jacquet²⁶, M. Jaffre²⁶, L. Janauschek²⁵, X. Janssen⁴, V. Jemanov¹¹, L. Jönsson²⁰,
 C. Johnson³, D.P. Johnson⁴, M.A.S. Jones¹⁸, H. Jung^{20,10}, D. Kant¹⁹, M. Kapichine⁸,
 M. Karlsson²⁰, O. Karschnick¹¹, J. Katzy¹⁰, F. Keil¹⁴, N. Keller³⁷, J. Kennedy¹⁸, I.R. Kenyon³,
 C. Kiesling²⁵, P. Kjellberg²⁰, M. Klein³⁵, C. Kleinwort¹⁰, T. Kluge¹, G. Knies¹⁰, B. Koblitz²⁵,
 S.D. Kolya²¹, V. Korbel¹⁰, P. Kostka³⁵, R. Koutouev¹², A. Koutov⁸, J. Kroseberg³⁷,
 K. Krüger¹⁰, T. Kuhr¹¹, D. Lamb³, M.P.J. Landon¹⁹, W. Lange³⁵, T. Laštovička^{35,30},
 P. Laycock¹⁸, E. Lebailly²⁶, A. Lebedev²⁴, B. Leißner¹, R. Lemrani¹⁰, V. Lendermann¹⁰,
 S. Levonian¹⁰, B. List³⁶, E. Lobodzinska^{10,6}, B. Lobodzinski^{6,10}, A. Loginov²³,
 N. Loktionova²⁴, V. Lubimov²³, S. Lüders³⁷, D. Lüke^{7,10}, L. Lytkin¹², N. Malden²¹,
 E. Malinovski²⁴, S. Mangano³⁶, P. Marage⁴, J. Marks¹³, R. Marshall²¹, H.-U. Martyn¹,
 J. Martyniak⁶, S.J. Maxfield¹⁸, D. Meer³⁶, A. Mehta¹⁸, K. Meier¹⁴, A.B. Meyer¹¹, H. Meyer³³,
 J. Meyer¹⁰, S. Michine²⁴, S. Mikocki⁶, D. Milstead¹⁸, S. Mohrdieck¹¹, M.N. Mondragon⁷,
 F. Moreau²⁷, A. Morozov⁸, J.V. Morris⁵, K. Müller³⁷, P. Murín^{16,42}, V. Nagovizin²³,
 B. Naroska¹¹, J. Naumann⁷, Th. Naumann³⁵, P.R. Newman³, F. Niebergall¹¹, C. Niebuhr¹⁰,
 O. Nix¹⁴, G. Nowak⁶, M. Nozicka³⁰, B. Olivier¹⁰, J.E. Olsson¹⁰, D. Ozerov²³, V. Panassik⁸,
 C. Pascaud²⁶, G.D. Patel¹⁸, M. Peez²², E. Perez⁹, A. Petrukhin³⁵, J.P. Phillips¹⁸, D. Pitzl¹⁰,
 R. Pöschl²⁶, I. Potachnikova¹², B. Povh¹², J. Rauschenberger¹¹, P. Reimer²⁹, B. Reisert²⁵,
 C. Risler²⁵, E. Rizvi³, P. Robmann³⁷, R. Roosen⁴, A. Rostovtsev²³, S. Rusakov²⁴, K. Rybicki⁶,
 D.P.C. Sankey⁵, E. Sauvan²², S. Schätzel¹³, J. Scheins¹⁰, F.-P. Schilling¹⁰, P. Schleper¹⁰,
 D. Schmidt³³, D. Schmidt¹⁰, S. Schmidt²⁵, S. Schmitt¹⁰, M. Schneider²², L. Schoeffel⁹,
 A. Schöning³⁶, T. Schörner-Sadenius²⁵, V. Schröder¹⁰, H.-C. Schultz-Coulon⁷,
 C. Schwanenberger¹⁰, K. Sedlák²⁹, F. Sefkow³⁷, I. Sheviakov²⁴, L.N. Shtarkov²⁴, Y. Sirois²⁷,
 T. Sloan¹⁷, P. Smirnov²⁴, Y. Soloviev²⁴, D. South²¹, V. Spaskov⁸, A. Specka²⁷, H. Spitzer¹¹,
 R. Stamen⁷, B. Stella³¹, J. Stiewe¹⁴, I. Strauch¹⁰, U. Straumann³⁷, S. Tchetchelnitski²³,
 G. Thompson¹⁹, P.D. Thompson³, F. Tomasz¹⁴, D. Traynor¹⁹, P. Truöl³⁷, G. Tsipolitis^{10,38},

I. Tsurin³⁵, J. Turnau⁶, J.E. Turney¹⁹, E. Tzamariudaki²⁵, A. Uraev²³, M. Urban³⁷, A. Usik²⁴, S. Valkár³⁰, A. Valkárová³⁰, C. Vallée²², P. Van Mechelen⁴, A. Vargas Trevino⁷, S. Vassiliev⁸, Y. Vazdik²⁴, C. Veelken¹⁸, A. Vest¹, A. Vichnevski⁸, V. Volchinski³⁴, K. Wacker⁷, J. Wagner¹⁰, R. Wallny³⁷, B. Waugh²¹, G. Weber¹¹, R. Weber³⁶, D. Wegener⁷, C. Werner¹³, N. Werner³⁷, M. Wessels¹, S. Wiesand³³, M. Winde³⁵, G.-G. Winter¹⁰, Ch. Wissing⁷, M. Wobisch¹⁰, E.-E. Woehrling³, E. Wünsch¹⁰, A.C. Wyatt²¹, J. Žáček³⁰, J. Zálešák³⁰, Z. Zhang²⁶, A. Zhokin²³, F. Zomer²⁶, and M. zur Nedden²⁵

¹ *I. Physikalisches Institut der RWTH, Aachen, Germany^a*

² *III. Physikalisches Institut der RWTH, Aachen, Germany^a*

³ *School of Physics and Space Research, University of Birmingham, Birmingham, UK^b*

⁴ *Inter-University Institute for High Energies ULB-VUB, Brussels; Universiteit Antwerpen (UIA), Antwerpen; Belgium^c*

⁵ *Rutherford Appleton Laboratory, Chilton, Didcot, UK^b*

⁶ *Institute for Nuclear Physics, Cracow, Poland^d*

⁷ *Institut für Physik, Universität Dortmund, Dortmund, Germany^a*

⁸ *Joint Institute for Nuclear Research, Dubna, Russia*

⁹ *CEA, DSM/DAPNIA, CE-Saclay, Gif-sur-Yvette, France*

¹⁰ *DESY, Hamburg, Germany*

¹¹ *Institut für Experimentalphysik, Universität Hamburg, Hamburg, Germany^a*

¹² *Max-Planck-Institut für Kernphysik, Heidelberg, Germany*

¹³ *Physikalisches Institut, Universität Heidelberg, Heidelberg, Germany^a*

¹⁴ *Kirchhoff-Institut für Physik, Universität Heidelberg, Heidelberg, Germany^a*

¹⁵ *Institut für experimentelle und Angewandte Physik, Universität Kiel, Kiel, Germany*

¹⁶ *Institute of Experimental Physics, Slovak Academy of Sciences, Košice, Slovak Republic^{e,f}*

¹⁷ *School of Physics and Chemistry, University of Lancaster, Lancaster, UK^b*

¹⁸ *Department of Physics, University of Liverpool, Liverpool, UK^b*

¹⁹ *Queen Mary and Westfield College, London, UK^b*

²⁰ *Physics Department, University of Lund, Lund, Sweden^g*

²¹ *Physics Department, University of Manchester, Manchester, UK^b*

²² *CPPM, CNRS/IN2P3 - Univ Mediterranee, Marseille - France*

²³ *Institute for Theoretical and Experimental Physics, Moscow, Russia^l*

²⁴ *Lebedev Physical Institute, Moscow, Russia^e*

²⁵ *Max-Planck-Institut für Physik, München, Germany*

²⁶ *LAL, Université de Paris-Sud, IN2P3-CNRS, Orsay, France*

²⁷ *LPNHE, Ecole Polytechnique, IN2P3-CNRS, Palaiseau, France*

²⁸ *LPNHE, Universités Paris VI and VII, IN2P3-CNRS, Paris, France*

²⁹ *Institute of Physics, Academy of Sciences of the Czech Republic, Praha, Czech Republic^{e,i}*

³⁰ *Faculty of Mathematics and Physics, Charles University, Praha, Czech Republic^{e,i}*

³¹ *Dipartimento di Fisica Università di Roma Tre and INFN Roma 3, Roma, Italy*

³² *Paul Scherrer Institut, Villigen, Switzerland*

³³ *Fachbereich Physik, Bergische Universität Gesamthochschule Wuppertal, Wuppertal, Germany*

³⁴ *Yerevan Physics Institute, Yerevan, Armenia*

³⁵ *DESY, Zeuthen, Germany*

³⁶ *Institut für Teilchenphysik, ETH, Zürich, Switzerland^j*

³⁷ *Physik-Institut der Universität Zürich, Zürich, Switzerland^j*

³⁸ *Also at Physics Department, National Technical University, Zografou Campus, GR-15773 Athens, Greece*

³⁹ *Also at Rechenzentrum, Bergische Universität Gesamthochschule Wuppertal, Germany*

⁴⁰ *Also at Institut für Experimentelle Kernphysik, Universität Karlsruhe, Karlsruhe, Germany*

⁴¹ *Also at Dept. Fis. Ap. CINVESTAV, Mérida, Yucatán, México^k*

⁴² *Also at University of P.J. Šafárik, Košice, Slovak Republic*

⁴³ *Also at CERN, Geneva, Switzerland*

⁴⁴ *Also at Dept. Fis. CINVESTAV, México City, México^k*

^a *Supported by the Bundesministerium für Bildung und Forschung, FRG, under contract numbers 05 H1 IGUA /1, 05 H1 IPAA /1, 05 H1 IPAB /9, 05 H1 IPEA /6, 05 H1 IVHA /7 and 05 H1 IVHB /5*

^b *Supported by the UK Particle Physics and Astronomy Research Council, and formerly by the UK Science and Engineering Research Council*

^c *Supported by FNRS-FWO-Vlaanderen, IISN-IKW and IWT*

^d *Partially Supported by the Polish State Committee for Scientific Research, grant no. 2P0310318 and SPUB/DESY/P03/DZ-1/99 and by the German Bundesministerium für Bildung und Forschung*

^e *Supported by the Deutsche Forschungsgemeinschaft*

^f *Supported by VEGA SR grant no. 2/1169/2001*

^g *Supported by the Swedish Natural Science Research Council*

ⁱ *Supported by the Ministry of Education of the Czech Republic under the projects INGO-LA116/2000 and LN00A006, by GAUK grant no 173/2000*

^j *Supported by the Swiss National Science Foundation*

^k *Supported by CONACyT*

^l *Partially Supported by Russian Foundation for Basic Research, grant no. 00-15-96584*

1 Introduction

At HERA, the interaction of protons with quasi-real photons emitted from the electron¹ beam can result in the production of jets [1, 2], for which two types of process are responsible in leading order (LO) quantum chromodynamics (QCD). The photon may interact as a pointlike particle with a parton carrying a fraction x_p of the proton momentum, in so-called direct processes (Fig. 1(a)). Alternatively, in resolved processes (Fig. 1(b)), the photon may develop a hadronic structure so that a parton carrying a fraction x_γ of the photon momentum interacts with a parton in the proton. Due to confinement, the partons emerging from the interaction fragment into jets of colourless particles. The hadronic final state also includes the proton remnant and, in the case of resolved processes, the photon remnant and additional particles resulting from possible remnant-remnant interactions (the underlying event).

The main purpose of this paper is to present inclusive jet cross sections measured using the H1 detector and to compare them with fixed order parton level QCD predictions. After correcting the data and calculations to the hadron level, these comparisons offer a means of testing the validity of perturbative QCD predictions, including the description of the partonic structure of the photon and the proton in terms of parton distribution functions (PDFs). The QCD-inspired modelling of non-perturbative effects in hard hadronic photoproduction can be tested as well. The most accurate theoretical predictions have been calculated up to next-to-leading order (NLO) in perturbative QCD. In order to compare these predictions with jet cross section measurements, the jet definition must meet certain requirements, such as infrared and collinear safety and minimal sensitivity to fragmentation and underlying event effects. The k_\perp algorithm, originally proposed in [3], satisfies these requirements.

Inclusive jet measurements at hadron colliders [4–8] and at HERA [9–13] have often been important in the development of the understanding of QCD. In this paper, the first H1 measurement of inclusive jet cross sections in photoproduction using the inclusive k_\perp algorithm [14] is presented. Compared with the last H1 inclusive jet measurement [11], the integrated luminosity has been increased by a factor of 80 and the jet transverse energy range has been extended, now reaching from 5 to 75 GeV. In order to allow cross-checks with previous HERA measurements and comparisons with data from other colliders, the measurements have also been performed using a cone algorithm.

The paper is organized as follows. In section 2, the motivations for this measurement are detailed and the phenomenology of inclusive jet photoproduction is presented. A brief description of the H1 detector and details of the analysis procedure are given in section 3. The measurements of single- and multi-differential inclusive jet cross sections as functions of jet transverse energy E_T^{jet} and pseudorapidity² η^{jet} in the laboratory frame are presented in section 4. The results are compared with LO and NLO QCD calculations and with inclusive jet measurements at $p\bar{p}$ colliders. The final section provides a summary of the results.

¹In the data taking periods used for this analysis, HERA was operated with a positron beam. However, the generic name “electron” will be used here to mean both electron and positron.

²Pseudorapidity is defined as $\eta \equiv -\ln(\tan \theta/2)$, where θ is the polar angle, in the coordinate system centered at the nominal interaction point, with respect to the positive z axis along the outgoing proton beam direction. The outgoing proton (photon) direction is also called forward (backward) and corresponds to $\eta > 0$ ($\eta < 0$).

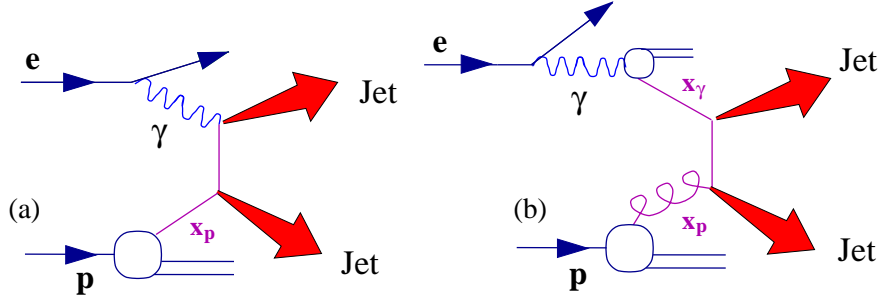


Figure 1: Example LO QCD diagrams for inclusive jet photoproduction in direct (a) and resolved (b) photon interactions.

2 Inclusive jet photoproduction

Inclusive jet cross sections are obtained by counting the number of jets found by a jet algorithm in a given kinematic range. The inclusive k_{\perp} algorithm [14] is a modified version of the exclusive k_{\perp} algorithm [15] where all hadronic final state particles are clustered iteratively³ into jets according to their separations in (η, ϕ) space⁴. Here, the algorithm is applied in the laboratory frame. The separation parameter between jets in (η, ϕ) space is set to $D = 1$, as in [17]. An E_T weighted recombination scheme [18], in which the reconstructed jets are massless, is used to maintain invariance under longitudinal boosts. To allow comparisons of the results of this study with previous measurements in photoproduction and with other collider data, the complete analysis has also been performed using a cone algorithm [19] with a cone radius $R = 1$. The cone algorithm has been shown to give larger hadronisation corrections than the inclusive k_{\perp} algorithm (section 2.4), as is the case for jets in deep inelastic scattering (DIS) [20].

2.1 Motivation

In this paper, inclusive jet cross sections are measured over a very large E_T^{jet} range. In the high E_T^{jet} region, the high transverse momentum of the outgoing parton provides a hard scale which allows reliable cross section calculations to be made in perturbative QCD. It also ensures a reduced influence of less-well understood soft processes (fragmentation and underlying event). Jets at high E_T^{jet} thus provide the most direct insight into photoproduction at the parton level.

In the region of low E_T^{jet} , the NLO and higher order terms as well as corrections from the parton to the hadron level become more important, since the strong coupling α_S increases with decreasing scale. In the absence of a fundamental understanding of non-perturbative processes, the comparisons between data and theory necessarily involve phenomenological models. Matching the theoretical predictions with the experimental measurements at low E_T^{jet} thus represents a further important test of QCD-inspired phenomenology in jet photoproduction.

Jet photoproduction cross sections are directly sensitive to the gluon as well as the quark content of the photon and the proton. The proton PDFs are precisely determined [21–23] from structure

³For more details, see e.g. [16].

⁴ ϕ is the azimuthal angle in the transverse plane.

function measurements [24, 25]. An exception is the gluon distribution at high x_p [26]. There, jet photoproduction measurements [17, 27] can provide complementary information. For the photon, the quark density at medium and high x_γ is constrained [28–30] by F_2^γ measurements at e^+e^- colliders [31], albeit with larger uncertainties than in the proton case. Since boson-gluon fusion is a higher order process compared with photon-quark scattering at e^+e^- colliders, the gluon density in the photon is even less well constrained. Furthermore, the photon PDFs do not obey strict momentum sum rules, so that there is no indirect constraint on the gluon density in the photon. In photoproduction at HERA, higher scales can be reached than at LEP because of the higher centre-of-mass (cms) energy and higher γp compared with $\gamma\gamma$ luminosity. Jet photoproduction cross section measurements [13, 17, 27, 32] thus access a largely unexplored domain of photon structure.

The measurement presented here probes a wide range of E_T^{jet} and η^{jet} , quite similar to the range explored in a recent dijet cross section measurement [17]. Although dijet events offer better constraints on the hard scattering kinematics, inclusive jet measurements offer the experimental advantages of greater statistics and increased kinematic range and the theoretical advantage of naturally avoiding infrared-sensitive regions of phase space [33].

2.2 QCD calculations

By considering the electron as a source of quasi-real photons of virtuality⁵ Q^2 and energy E_γ and using the QCD factorisation theorem and a factorisable jet algorithm, the electron-proton cross section for producing N jets ($N \geq 2$) in direct photoproduction can be expressed as:

$$\sigma_{\text{dir.}}^{ep \rightarrow e + N \text{ jets} + X} = \int_{\Omega} d\Omega f_{\gamma/e}(y, Q^2) \sum_i f_{i/p}(x_p, \mu_p^2) d\hat{\sigma}(\gamma i \rightarrow N \text{ jets}) . \quad (1)$$

Here, $y = E_\gamma/E_e$ is the fraction of the electron energy E_e carried by the photon, $f_{\gamma/e}(y, Q^2)$ is the photon flux associated with the electron [34], $f_{i/p}(x_p, \mu_p^2)$ is the proton PDF of parton i evaluated at the factorisation scale μ_p and $\hat{\sigma}(\gamma i \rightarrow N \text{ jets})$ is the parton-level cross section for the direct subprocess $\gamma i \rightarrow N \text{ jets}$. The cross section $\hat{\sigma}$ is proportional to $\alpha_{em}(\mu_R^2)\alpha_S^{N-1}(\mu_R^2)$ at lowest order and can be expanded in powers of α_S multiplied by perturbatively calculable coefficient functions, both of which depend on the renormalisation scale μ_R . The kinematic domain over which the cross section is integrated is denoted Ω .

Similarly, the cross section for resolved photoproduction can be written:

$$\sigma_{\text{res.}}^{ep \rightarrow e + N \text{ jets} + X} = \int_{\Omega} d\Omega f_{\gamma/e}(y, Q^2) \sum_{ij} f_{i/p}(x_p, \mu_p^2) f_{j/\gamma}(x_\gamma, \mu_\gamma^2) d\hat{\sigma}(ij \rightarrow N \text{ jets}) . \quad (2)$$

Compared with Eq. 1 for direct processes, the resolved cross section in Eq. 2 includes in addition the photon PDF of parton j , $f_{j/\gamma}(x_\gamma, \mu_\gamma^2)$, evaluated at the factorisation scale μ_γ . Due to the splitting $\gamma \rightarrow q\bar{q}$, the QCD evolution equations of the resolved photon PDFs [35] differ from those for the proton and lead to large quark densities at high x_γ , which increase with μ_γ . The cross section $\hat{\sigma}(ij \rightarrow N \text{ jets})$ describes the resolved subprocess $ij \rightarrow N \text{ jets}$ and is proportional to $\alpha_S^N(\mu_R^2)$ at lowest order.

⁵The photon virtuality is $Q^2 \equiv -(k - k')^2$, where k (k') is the 4-vector of the incoming (outgoing) electron.

The distinction between the direct (Eq. 1) and the resolved (Eq. 2) components is only unambiguous at LO, whereas beyond LO their relative contributions depend on the factorisation scale μ_γ . The inclusive cross section for the production of a jet in a given kinematic range $\sigma^{ep \rightarrow e + \text{jet} + X}$ is obtained by summing all calculated contributions of Eqs. 1 and 2 over N , weighting by the corresponding number of jets inside this kinematic range.

The partonic cross sections $\hat{\sigma}$ in Eqs. 1 and 2 have been calculated at LO and NLO in QCD by several theoretical groups [33, 36–38]. These calculations differ mainly in the treatment of infrared and collinear singularities. In this paper, measurements are compared with the LO and NLO calculations of [33], based on the subtraction method as implemented in a Monte Carlo program [39]. This program generates weighted parton kinematic configurations used as input to the inclusive k_\perp algorithm. These calculations differ from those obtained with the phase space slicing method [38] by less than 2 % [40].

The CTEQ5M [21] parameterisation of the proton PDFs was used for the calculations. To test the dependence of the NLO cross sections on the choice of proton PDFs, MRST99 [22] and CTEQ5HJ [21] were also used, where the latter has an enhanced gluon distribution at high x_p . The renormalisation group equation to 2-loop accuracy was used for α_S and the value of Λ_{QCD} was chosen to match that used in the evolution of the proton PDFs (for five quark flavours, $\alpha_S(M_Z) = 0.118$ for CTEQ5M and CTEQ5HJ, $\alpha_S(M_Z) = 0.1175$ for MRST99). GRV-HO [29] was chosen as the standard parameterisation of the photon PDFs. The AFG-HO [30] parameterisation was also used to study the dependence of the results on the choice of photon PDFs. The renormalisation and factorisation scales were defined as the sum of the transverse energies of the outgoing partons divided by 2. These scales were varied by factors 0.5 and 2 in order to estimate the uncertainty corresponding to the missing higher-order terms.

2.3 Monte Carlo models

Simulated event samples have been used to correct the data for detector effects (section 3.3) and to estimate hadronisation effects for the QCD calculations (section 2.4). Direct and resolved photoproduction events were simulated using the PYTHIA [41], HERWIG [42], and PHOJET [43] Monte Carlo generators. The generated events were passed through a GEANT [44] simulation of the H1 detector and the same reconstruction chain as the data.

All programs generate partonic interactions using the Born level QCD hard scattering matrix elements, regulated by a minimum cut-off \hat{p}_T^{min} on the common transverse momentum of the two outgoing partons. For PYTHIA and PHOJET (HERWIG), the strong coupling constant α_S was calculated by solving the 1 (2) loop renormalisation group equation using $\Lambda_{\text{QCD}} = 200$ MeV for 4 (5) quark flavours. GRV-LO parameterisations of the proton [23] and the photon [28] PDFs were used. Higher order QCD radiation effects are simulated through initial and final state parton showers in the leading log approximation. The fragmentation process is performed using the Lund string model [45] as implemented in JETSET [46] in the case of PYTHIA and PHOJET and using a cluster model [47] in the case of HERWIG.

For resolved photon interactions, besides the primary parton-parton scattering, additional interactions are generated in order to simulate the effect of the underlying event. Within PYTHIA, these are calculated as LO QCD processes between partons from the remnants of the proton

and the photon. The resulting additional final state partons are required to have transverse momenta above 1.2 GeV, a value which gives an optimal description of the transverse energy flow outside jets for the specific photon PDFs used [11]. Soft particles accompanying the hard subprocess are produced in HERWIG using a soft underlying event (SUE) mechanism which is based on parameterisations of experimental results on soft hadron-hadron collisions. The fraction of resolved interactions which are generated with an additional SUE can be varied within HERWIG and has been adjusted to 35 % to match the observed level of soft activity between jets. PHOJET, which is based on the two-component dual parton model [48] incorporates detailed simulations of multiple soft and hard parton interactions on the basis of a unitarisation scheme. Due to this scheme, small variations of the lower momentum cut-off for hard parton interactions, set here to $\hat{p}_T^{\min} = 3$ GeV, do not have an influence on the results of this generator.

2.4 Hadronisation corrections

Since the QCD calculations refer to jets of partons, whereas the measurements refer to jets of hadrons, the predicted cross sections have been corrected to the hadron level using LO Monte Carlo programs. The hadronisation correction factors, $(1 + \delta_{hadr.})$, are defined as the ratio of the cross sections obtained with jets reconstructed from hadrons after the full event simulation (including parton showers, fragmentation and underlying event effects) to that from partons after parton showers but before fragmentation and underlying event simulation. These corrections were calculated by taking the results from two different Monte Carlo models chosen as described in section 3.3. The uncertainty on these corrections was taken as the quadratic sum of the statistical error and the systematic error given by half the difference between the results obtained from the two Monte Carlo models. Using the k_\perp algorithm, the corrections were found to be approximately 30 % for $E_T^{jet} < 10$ GeV falling to values typically below 12 % for $E_T^{jet} > 20$ GeV. With the cone algorithm, the corrections are around 40 % for $E_T^{jet} < 15$ GeV and 20 % for $E_T^{jet} > 15$ GeV. The difference between the results obtained with the two Monte Carlo models is typically very small and at most 10 %.

The effects of the underlying event and of the fragmentation were also studied separately. The corresponding correction factors, $(1 + \delta_{u.e.})$ and $(1 + \delta_{frag.})$, were determined in the same way as the overall corrections factors $(1 + \delta_{hadr.})$. Here, $(1 + \delta_{u.e.})$ is defined as the ratio of the cross sections obtained with jets reconstructed from hadrons with simulation of the underlying event to that from hadrons without simulation of the underlying event, whilst $(1 + \delta_{frag.})$ is defined as the ratio of the cross sections obtained with jets reconstructed from hadrons to that from partons after parton showers, both without simulation of the underlying event. By definition, $(1 + \delta_{hadr.}) = (1 + \delta_{u.e.}) \cdot (1 + \delta_{frag.})$.

Low momentum hadrons from the underlying event lead to a systematic increase of E_T^{jet} and thus of the hadron level cross section at fixed E_T^{jet} . The $\delta_{u.e.}$ correction is always positive and increases as E_T^{jet} decreases or η^{jet} increases. Using the inclusive k_\perp algorithm, for $5 \leq E_T^{jet} < 12$ GeV, $\delta_{u.e.}$ varies between ~ 30 % at $\eta^{jet} = -0.75$ and 100 % at $\eta^{jet} = 1.25$. For $E_T^{jet} > 20$ GeV, $\delta_{u.e.}$ is always below 10 %. The effect of the underlying event is partially compensated by fragmentation, which has a tendency to lower the cross section. In general, $\delta_{frag.}$ is negative and becomes more important as E_T^{jet} decreases but also as η^{jet} decreases, in contrast to $\delta_{u.e.}$. The $\delta_{frag.}$ correction is around -30 % for $5 \leq E_T^{jet} < 12$ GeV and around -5 % for $E_T^{jet} \geq 20$ GeV.

3 Experimental technique

3.1 H1 detector

A detailed description of the H1 detector can be found elsewhere [49]. Here only the components relevant for this measurement are briefly described.

The ep luminosity is determined with a precision of 1.5 % by comparing the event rate in the photon detector, located at $z = -103$ m, with the cross section for the QED bremsstrahlung process $ep \rightarrow ep\gamma$. The scattered electron may be detected in the electron tagger (ETag), located at $z = -33$ m. Both detectors are TlCl/TlBr crystal Čerenkov calorimeters with an energy resolution of $22\%/\sqrt{E/\text{GeV}}$.

The central tracker (CT), which covers the range $|\eta| \leq 1.5$ is used to measure the trajectories of charged particles and to reconstruct the interaction vertex. It consists of inner and outer cylindrical jet chambers for precise position measurement in the transverse plane, z -drift chambers for precise z measurement and proportional chambers for triggering purposes. The transverse momentum of charged particles is reconstructed from the curvature of tracks in the homogeneous magnetic field of 1.15 Tesla along the beam direction, with a resolution $\sigma(p_T)/p_T \approx 0.6\% p_T/\text{GeV}$.

The finely segmented Liquid Argon (LAr) calorimeter [50] surrounds the tracking system and covers the range $-1.5 \leq \eta \leq 3.4$ with full azimuthal acceptance. It consists of an electromagnetic section with lead absorbers and a hadronic section with steel absorbers. The total depth of the LAr calorimeter ranges from 4.5 to 8 hadronic interaction lengths. The energy resolution determined in test beam measurements is $\sigma(E)/E \approx 50\%/\sqrt{E/\text{GeV}} \oplus 2\%$ for charged pions. For jets with E_T^{jet} above 20 GeV, the jet energy calibration agrees at the 2 % level with the Monte Carlo simulation, as determined by the E_T balance in neutral current (NC) DIS and jet photoproduction events. At lower E_T^{jet} , the absolute hadronic energy scale is known to 4 %. The absolute resolution in η^{jet} is approximately 0.05 at $E_T^{jet} = 5$ GeV and better than 0.02 for $E_T^{jet} > 20$ GeV.

The region $-4.0 \leq \eta \leq -1.4$ is covered by the SPACAL lead/scintillating-fibre calorimeter [51]. Its absolute hadronic energy scale is known to 7 %.

3.2 Event selection and reconstruction

The data used in this paper were collected in 1996 and 1997, when electrons of energy $E_e = 27.5$ GeV collided with protons of energy $E_p = 820$ GeV, resulting in an ep cms energy of 300 GeV. For measurements in the region $E_T^{jet} \geq 21$ GeV (“high” E_T^{jet}), the full data sample representing an integrated luminosity of 24.1 pb^{-1} was used. In addition to some activity in the central region, as seen by the CT, the trigger conditions required high transverse energy deposits in the LAr calorimeter (jet triggers). In the region $5 \leq E_T^{jet} < 21$ GeV (“low” E_T^{jet}), where jet triggers suffer from proton beam-induced background, a trigger based on scattered electron signals in the ETag was used instead. This trigger was operated during a ‘minimum bias’ data taking period corresponding to an integrated luminosity of 0.47 pb^{-1} . The events from this

subsample were required to have the scattered electron detected in the fiducial volume of the ETag, with an energy in the range $9.6 \leq E'_e \leq 19.3$ GeV. The ETag geometrical acceptance, which is corrected for on an event-by-event basis, is always greater than 10 % in this range. The detection of the scattered electron ensures an improved measurement of y and hence of the photon-proton cms energy $W_{\gamma p} = \sqrt{4yE_eE_p}$, but reduces the available number of events by a factor of approximately ten, due to the restricted y range and to the limited acceptance of the ETag. The ETag events were also required to have no energy deposited in the photon arm of the luminosity system. This condition suppresses background from high rate Bethe-Heitler events in random coincidence with proton beam-induced background events which give activity in the interaction region. It also reduces QED radiative corrections.

An interaction vertex, reconstructed from tracks in the CT and located within 30 cm of the nominal z position of the interaction point, was demanded. Energy deposits in the calorimeters and tracks in the CT were combined, in a manner that avoids double counting, in order to optimize the reconstruction of the hadronic final state [52], from which $W_{\gamma p}$ was derived [53] for the “high” E_T^{jet} analysis. The inclusive jet sample was then defined by keeping all events for which at least one jet was reconstructed with the inclusive k_\perp algorithm in the kinematic domain:

$$-1 \leq \eta^{jet} \leq 2.5 ; E_T^{jet} \geq 21 \text{ GeV} \text{ (“high” } E_T^{jet}) ; \quad (3)$$

$$-1 \leq \eta^{jet} \leq 2.5 ; E_T^{jet} \geq 5 \text{ GeV} \text{ (“low” } E_T^{jet}). \quad (4)$$

The η^{jet} range was chosen to ensure that the jets were well contained in the LAr calorimeter. For “high” E_T^{jet} events, the kinematic region was restricted to

$$Q^2 \leq 1 \text{ GeV}^2 ; 95 \leq W_{\gamma p} \leq 285 \text{ GeV}. \quad (5)$$

The Q^2 range is implied by the absence of the scattered electron in the main H1 detector. For “low” E_T^{jet} events, the tagging of the electron already restricted the kinematic region to

$$Q^2 \leq 10^{-2} \text{ GeV}^2 ; 164 \leq W_{\gamma p} \leq 242 \text{ GeV}. \quad (6)$$

A number of requirements were made in order to suppress the non- ep background. For “high” E_T^{jet} , the vertex condition was sufficient to reduce the contamination from beam-induced background to a negligible level. Background originating from cosmic showers and beam halo muons was rejected using a set of topological muon finders [54]. In addition, the total missing transverse momentum \cancel{P}_T was required to be small compared with the total transverse energy E_T by applying the cut $\cancel{P}_T/\sqrt{E_T} \leq 2.5 \text{ GeV}^{\frac{1}{2}}$. The overall non- ep background contamination in the “high” E_T^{jet} sample was then estimated to be below 1 %. For “low” E_T^{jet} events, since $W_{\gamma p}$ can be measured in two independent ways (using either the energy of the scattered electron or the hadronic final state), consistency between the results of the two methods was required. By fitting the distribution of the z position of the vertex with the sum of a Gaussian and a constant, the “low” E_T^{jet} sample was estimated to have a non- ep background contamination of about 2 %.

Further cuts were applied to reduce backgrounds from other ep collision processes. For the “high” E_T^{jet} jet sample, the only significant one is the NC DIS process⁶, where either the scattered electron or the current jet enters the inclusive jet selection. Events with a scattered electron

⁶The charged current DIS background was already completely suppressed by the \cancel{P}_T cut.

candidate found using electron identification algorithms [25] were thus rejected. The remaining ep background in the “high” E_T^{jet} sample was estimated to be below 1 % from a study using a simulated sample of NC DIS events from the DJANGO [55] Monte Carlo generator. In the “low” E_T^{jet} sample it is completely negligible.

The event samples finally consist of 15 388 jets reconstructed in 11 801 events for “high” E_T^{jet} and 26 848 jets reconstructed in 21 001 events for “low” E_T^{jet} . For both samples, the total background of around 2 % was subtracted. The inefficiency due to selection cuts is below 3 %.

3.3 Cross section determination

To obtain the inclusive jet cross section, each of the N jets reconstructed in a given range is assigned a weight calculated as the inverse of the event-by-event trigger efficiency ϵ . The cross section obtained at the detector level is then corrected by a factor \mathcal{C} for inefficiencies due to the selection procedure and for migrations caused by the detector response. For instance, the double-differential cross section averaged over a range $\Delta E_T^{jet} \Delta \eta^{jet}$, is defined as:

$$\frac{d^2 \sigma^{ep \rightarrow e + jet + X}}{dE_T^{jet} d\eta^{jet}} = \frac{\sum_{i=1}^N (\frac{1}{\epsilon_i})}{\Delta E_T^{jet} \Delta \eta^{jet} \mathcal{C} \mathcal{L}} \quad (7)$$

where \mathcal{L} is the integrated luminosity.

The trigger efficiency ϵ was determined from data by using events triggered independently. For the “high” E_T^{jet} analysis, ϵ was parameterised as a function of the E_T and η of the leading jet and was always greater than 80 %, reaching 100 % for $E_T \geq 35$ GeV. For the “low” E_T^{jet} analysis, ϵ was found to depend on the multiplicity of CT tracks in the event, with a mean value of 97 %.

Two Monte Carlo programs (section 2.3) were used to correct the data from each event sample for detector effects. For the “high” E_T^{jet} sample, HERWIG and PYTHIA were chosen. A reasonable description of the observed energy flow around the jet axis was obtained with both programs, provided the underlying event or multiple interaction mechanisms were included in the Monte Carlo simulations [40]. For the “low” E_T^{jet} sample, PHOJET, which has been shown to give the best description of energy flow distributions [11] and jet profiles [40], was chosen together with PYTHIA. The mean correction factors \mathcal{C} calculated for each measurement interval with the two Monte Carlo models were found to lie between 0.9 and 1.6 for the “high” E_T^{jet} analysis and between 0.5 and 1.6 for the “low” E_T^{jet} analysis.

The bin-to-bin migrations are important due to the steeply-falling shape of the E_T^{jet} spectrum. The bin widths were chosen to measure cross sections in as many intervals as possible whilst ensuring that stability and purity⁷ were greater than 30 %. These criteria restrict the η^{jet} cross section measurements to different η^{jet} ranges depending on the E_T^{jet} range considered. At “high” E_T^{jet} , the problematic region is that of negative η^{jet} . Due to the Lorentz boost between the γp cms and the laboratory frame, $\eta^{jet} = 0$ corresponds to a cms pseudorapidity⁸ η^* of about -2 , which is well into the photon hemisphere. The cross section thus falls most steeply with increasing E_T^{jet} in this region. At “low” E_T^{jet} , the influence of the proton remnant compromises measurements towards higher η^{jet} .

⁷The stability \mathcal{S} (purity \mathcal{P}) is defined as the number of jets which are both generated and reconstructed in an analysis bin, divided by the total number of jets that are generated (reconstructed) in that bin. By definition, $\mathcal{C} \equiv \mathcal{S}/\mathcal{P}$.

⁸ $\eta^* = \eta - \ln(2E_p/W_{\gamma p})$.

3.4 Systematic uncertainties

The following systematic uncertainties have been considered :

- The uncertainty in the absolute hadronic energy scale of the LAr calorimeter (2 % for “high” E_T^{jet} and 4 % for “low” E_T^{jet}) leads to an uncertainty of typically 10 % for “high” E_T^{jet} and between 10 % and 20 % for “low” E_T^{jet} .
- The 7 % uncertainty in the hadronic SPACAL energy scale results in an uncertainty of 1 % at “high” E_T^{jet} and is negligible at “low” E_T^{jet} .
- The 3 % uncertainty in the fraction of the energy of the reconstructed hadronic final state carried by tracks leads to an uncertainty of less than 1 % for “high” E_T^{jet} and of 2 % to 4 % for “low” E_T^{jet} .
- The background subtraction leads to an uncertainty of 1 %.
- The statistical uncertainty in the trigger efficiency determination leads to an uncertainty of 1 % or less.
- The uncertainty in the integrated luminosity results in an overall normalisation error of 1.5 %.
- The uncertainty in the correction for detector effects was taken to be half the difference between the correction factors calculated from the two Monte Carlo programs. It is smaller than 8 % for “high” E_T^{jet} and smaller than 10 % for “low” E_T^{jet} .

All systematic uncertainties are added in quadrature. The resulting uncertainty ranges from 10 % to 20 % for “high” E_T^{jet} and from 15 % to 30 % for “low” E_T^{jet} and is dominated by the normalisation uncertainty due to the LAr calorimeter energy scale.

4 Results

In this section, inclusive jet cross sections are presented, corrected for detector effects and measured in different kinematic regions as functions of E_T^{jet} and η^{jet} in the laboratory frame. Good agreement with previous data [9–12] has been found when using the cone algorithm [40]. The results are also consistent with recently published ZEUS data [13] using the k_\perp algorithm. The numerical results using the k_\perp algorithm (Tabs. 1 to 5) are given as differential cross sections averaged over the quoted ranges. Those obtained with the cone algorithm (Tabs. 6 and 7) are given at the average value in each analysis interval, determined according to the Monte Carlo simulation. The results are shown in Figs. 2 to 9. In the E_T^{jet} spectra (upper part of Figs. 2 to 4), all systematic uncertainties are added in quadrature with the statistical uncertainty and are shown as error bars. The inner error bars denote the statistical and the outer the total uncertainty. In all other figures, the LAr calorimeter energy scale uncertainty is not included in the error bars, but is shown separately as a hatched band. The results are compared with LO and NLO QCD predictions first, then with similar measurements at $p\bar{p}$ colliders. Unless otherwise

stated, the QCD prediction is calculated at NLO with the standard settings described in section 2.2 and corrected for hadronisation, as explained in section 2.4. Its uncertainty is shown as a shaded band divided into two parts. The inside (light) part is the uncertainty associated with the hadronisation corrections and the outside (dark) part is the uncertainty associated with the choice of the renormalisation and factorisation scales. These uncertainties are added linearly. When presented (Figs. 2 to 5), the relative differences are always defined with respect to this standard NLO QCD prediction. The total hadronisation correction factors $(1 + \delta_{hadr.})$ and their errors are given in the tables, together with the correction factors associated with the effects of fragmentation, $(1 + \delta_{frag.})$ and of the underlying event, $(1 + \delta_{u.e.})$.

4.1 E_T^{jet} cross sections

The measured differential e^+p cross section $d\sigma/dE_T^{jet}$ for inclusive jet production integrated over $-1 \leq \eta^{jet} \leq 2.5$ in the kinematic region defined by $Q^2 \leq 1 \text{ GeV}^2$ and $95 \leq W_{\gamma p} \leq 285 \text{ GeV}$ is shown for $E_T^{jet} > 21 \text{ GeV}$ in Fig. 2 (top). The LO QCD calculation fails to reproduce the normalisation of the distribution. Both NLO predictions, with and without hadronisation corrections, reproduce the measured distribution very well. As shown in Fig. 2 (bottom), the uncertainty due to the renormalisation and factorisation scales is of the order of 10 %. The calculated cross sections using the GRV photon PDFs are typically 5 % to 10 % larger than those obtained with AFG. To show the sensitivity to the proton PDFs, the predictions using GRV for the photon and MRST99 or CTEQ5HJ for the proton are also shown. Compared with CTEQ5M, MRST99 and CTEQ5HJ give almost the same prediction at relatively small E_T^{jet} , but show differences as E_T^{jet} increases. The prediction using MRST99 decreases relative to that using CTEQ5M by 5 % over the measured E_T^{jet} range while that using CTEQ5HJ increases by 8 %. Within the errors, the NLO QCD calculations with each of the PDFs choices describe the magnitude and the shape of the measured inclusive E_T^{jet} spectrum very well, up to the highest measured E_T^{jet} values.

In Fig. 3 (top), $d\sigma/dE_T^{jet}$ is presented for two separate $W_{\gamma p}$ intervals $95 \leq W_{\gamma p} < 212 \text{ GeV}$ and $212 \leq W_{\gamma p} \leq 285 \text{ GeV}$. At higher $W_{\gamma p}$, the E_T^{jet} spectrum is harder and extends to higher E_T^{jet} values, as expected. The predictions of the two combinations of photon and proton PDFs which give the lowest (AFG for the photon and MRST99 for the proton) and the highest (GRV for the photon and CTEQ5HJ for the proton) cross sections are also shown. As can be seen in Fig. 3 (bottom), all these NLO QCD calculations describe the magnitude and the shape of the inclusive E_T^{jet} spectra measured in the two $W_{\gamma p}$ ranges.

A measurement of the inclusive jet cross section over the whole E_T^{jet} range was performed by combining the “low” and “high” E_T^{jet} data samples. In order to do this, the same $W_{\gamma p}$ cut was applied to the “high” as to the “low” E_T^{jet} data sample, i.e. $164 \leq W_{\gamma p} \leq 242 \text{ GeV}$. The “low” E_T^{jet} cross section was also corrected to correspond to the same Q^2 range⁹ as the “high” E_T^{jet} sample. The measured cross section is shown in Fig. 4. The analyses of the “low” and “high” E_T^{jet} samples agree well in their domain of overlap. The measured $d\sigma/dE_T^{jet}$ cross

⁹The “low” E_T^{jet} cross section was multiplied by the ratio $R_F = F(1 \text{ GeV}^2)/F(0.01 \text{ GeV}^2)$, where $F(Q_{max}^2)$ is the integral of the photon flux $f_{\gamma/e}(y, Q^2)$ (see Eqs. 1 and 2) over $Q^2 < Q_{max}^2$ in the range $0.3 \leq y \leq 0.65$, which corresponds to the chosen $W_{\gamma p}$ range. The numerical integration yields $F(1 \text{ GeV}^2) = 0.0181$, $F(0.01 \text{ GeV}^2) = 0.0127$ and $R_F = 1.43$.

section falls by more than 6 orders of magnitude between $E_T^{jet} = 5$ and 75 GeV and is well reproduced by the theoretical prediction. The NLO contribution and the hadronisation corrections are both needed to give a good agreement of the calculation with the measured data.

Following a procedure previously applied to the inclusive charged particle photoproduction cross section [56], the power-law [57] function $\propto (1 + E_T^{jet}/E_{T,0})^{-n}$ was fitted to the inclusive jet cross section $1/E_T^{jet} \cdot d\sigma/dE_T^{jet}$ obtained from the data of Fig. 4. Good fits with stable results could only be obtained in the region $5 \leq E_T^{jet} < 35$ GeV. The fit gave the results $E_{T,0} = 2.4 \pm 0.6$ (stat.) $^{+0.2}_{-0.6}$ (syst.) GeV and $n = 7.5 \pm 0.3$ (stat.) $^{+0.1}_{-0.5}$ (syst.). The value of the exponent is in agreement with that obtained in [56]: $n = 7.03 \pm 0.07$ (stat.) ± 0.20 (syst.).

4.2 η^{jet} cross sections

The measured differential e^+p cross section $d\sigma/d\eta^{jet}$ in the range $-1 \leq \eta^{jet} \leq 2.5$ for inclusive jet production integrated over $21 \leq E_T^{jet} \leq 75$ GeV, $Q^2 \leq 1$ GeV² and $95 \leq W_{\gamma p} \leq 285$ GeV is shown in Fig. 5. The calculated cross sections using different combinations of the photon and proton PDFs give a good description of the data, within the experimental and theoretical errors. The normalisation of the data can only be described when the NLO contribution is included. The description is not significantly improved by the hadronisation corrections.

In Fig. 6, $d\sigma/d\eta^{jet}$ is presented in three different intervals of E_T^{jet} and compared with NLO QCD predictions. The hadronisation corrections correspond to an increase (decrease) of the pure partonic prediction in the forward (backward) region. The increase in the forward region is due to the influence of the proton remnant leading to significant underlying energy, while the decrease in the backward region reflects the escape of partonic energy from the jet due to fragmentation (section 2.4). Within the errors, the data are well described by the NLO QCD predictions.

In order to study the cross section more differentially, measurements of $d\sigma/d\eta^{jet}$ in two regions of $W_{\gamma p}$ and three intervals of E_T^{jet} are presented in Fig. 7. The maximum of the cross section is shifted towards low η^{jet} values at higher $W_{\gamma p}$ due to the decreased forward boost of the hadronic cms relative to the laboratory frame. The NLO QCD predictions with and without (not shown in Fig. 7) hadronisation corrections are in general in good agreement with the measured cross sections. NLO QCD calculations using different combinations of photon and proton PDFs also give good agreement with the data. The precision of the measurement as well as the theoretical uncertainties do not allow any firm conclusion to be drawn on which combination of PDFs is favoured by the data.

The $d\sigma/d\eta^{jet}$ measurement for the “low” E_T^{jet} sample is presented in Fig. 8 for two intervals of E_T^{jet} , in the kinematic region $Q^2 \leq 10^{-2}$ GeV² and $164 \leq W_{\gamma p} \leq 242$ GeV. The NLO predictions are in agreement with the data in the range $12 \leq E_T^{jet} \leq 21$ GeV, provided the hadronisation corrections are included. In the lowest E_T^{jet} range $5 \leq E_T^{jet} < 12$ GeV, however, the agreement with the NLO predictions including hadronisation corrections is marginal and the data seem to indicate a rise of the cross section with increasing η^{jet} which is faster than in the theoretical predictions. This may be the result of a failure of the LO Monte Carlo to accurately estimate the hadronisation corrections. Inadequacy of the photon PDFs in this kinematic range or the absence of higher order corrections beyond NLO may also be responsible.

4.3 Comparison with $p\bar{p}$ collider results

It is interesting to compare the present photoproduction measurements with similar $p\bar{p}$ data in order to see the effects arising from the different structure of the photon and the proton. The differential e^+p cross section $d\sigma/dE_T^{jet}$ was measured in the range $-1 \leq \eta^{jet} \leq 2.5$, as in Fig. 4, but using the cone algorithm with cone radius $R = 1$ to match the procedure used for the only available $p\bar{p}$ data [4] at comparable cms energy $\sqrt{s} = 200$ GeV. The results are presented in Tab. 6. Up to a normalisation factor, the E_T^{jet} dependence of the data is compatible in the region of overlap $5 \leq E_T^{jet} \leq 22$ GeV with that of [4]. Monte Carlo studies show that the difference in cms jet pseudorapidity ranges between the γp ($-3.0 \lesssim \eta^* \lesssim 0.5$) and $p\bar{p}$ ($|\eta^*| < 1.5$) data does not affect this conclusion.

To allow comparisons with $p\bar{p}$ measurements at different energies, the scaled γp cross section

$$S(x_T) \equiv E_T^{jet4} E_T^{jet} \frac{d^3\sigma}{dp^{jet3}} = \frac{E_T^{jet3}}{2\pi} \frac{d^2\sigma}{dE_T^{jet} d\eta^{jet}}, \quad (8)$$

where (E_T^{jet}, p_T^{jet}) is the four-vector of the jet, was measured as a function of the dimensionless variable $x_T = 2E_T^{jet}/W_{\gamma p}$. In the naive parton model, $S(x_T)$ is independent of cms energy for the same colliding particles. The differential e^+p cross section $d\sigma/dE_T^{jet}$ was measured with the cone algorithm in the restricted range $1.5 \leq \eta^{jet} \leq 2.5$ and $E_T^{jet} > 8$ GeV. It was then transformed into $S(x_T)$ at a fixed $W_{\gamma p} = 200$ GeV averaged over the range $|\eta^*| \leq 0.5$ using the Monte Carlo models to evaluate the correction factors and their uncertainties.

The $S(x_T)$ distribution is presented in Tab. 7 and Fig. 9. In the figure, it is compared with data from $p\bar{p}$ scattering obtained by the UA1 [4, 5] and D0 [6, 7] collaborations at various energies using the cone algorithm. The $p\bar{p}$ data were transformed into $S(x_T)$ using the E_T^{jet} value at the centre of each measurement interval and were scaled by factors of $\mathcal{O}(\alpha_{em}/\alpha_S)$ such that $S(x_T)$ approximately matches that from the photoproduction data at $x_T \sim 0.1$. Despite the differences in the η^* ranges of measurement and in the details of the analysis procedure¹⁰, all $p\bar{p}$ data are in approximate agreement after the scaling factors are applied. Within the experimental uncertainties, the shape of the $S(x_T)$ distribution for γp is compatible with those from $p\bar{p}$ data in the region $x_T \lesssim 0.2$, where the resolved photon leads to a similar behaviour of the scaled cross section to that for a hadron except for the overall normalisation. At larger x_T , the shape of the γp cross section begins to deviate from that for $p\bar{p}$. As can be inferred from the PYTHIA predictions for the full γp cross section and for the contribution from resolved photons, this is due to the enhancement of the resolved photon quark density relative to that of the proton at large momentum fractions, as well as the increasing proportion of direct photon interactions. The direct photon contribution involves the convolution of only one set of PDFs and dominates the scaled cross section at the largest x_T .

¹⁰UA1 measured cross sections in the range $|\eta^*| \leq 1.5$ for $\sqrt{s} = 200$ GeV and $|\eta^*| \leq 0.7$ for $\sqrt{s} = 630$ GeV, using a cone radius $R = 1$ and no jet pedestal energy subtraction. D0 measured cross sections in the range $|\eta^*| \leq 0.5$ using a cone radius $R = 0.7$ and jet pedestal energy subtraction.

5 Summary

A new measurement of inclusive jet production cross sections in quasi-real photoproduction ($Q^2 \leq 1 \text{ GeV}^2$) has been presented, based on an integrated luminosity of 24.1 pb^{-1} of e^+p data collected by the H1 experiment in the years 1996 and 1997. Compared with the last published H1 result [11] on this topic, this measurement represents an increase in luminosity by a factor of 80. The jets were selected using the inclusive k_\perp algorithm in the pseudorapidity range $-1 \leq \eta^{jet} \leq 2.5$ in the laboratory frame. The photon-proton centre-of-mass energy range of the measurement for jets with transverse energies $E_T^{jet} \geq 21 \text{ GeV}$ is $95 \leq W_{\gamma p} \leq 285 \text{ GeV}$. The measurement could be extended down to $E_T^{jet} \geq 5 \text{ GeV}$ by using a sample of data with integrated luminosity 0.47 pb^{-1} , collected in a data taking period with a dedicated trigger. There, the kinematic range of measurement was $Q^2 \leq 0.01 \text{ GeV}^2$ and $164 \leq W_{\gamma p} \leq 242 \text{ GeV}$.

The measured cross sections were corrected to the hadron level and compared with leading order (LO) and next-to-leading order (NLO) QCD calculations, with and without fragmentation and underlying event corrections. The LO QCD calculations are unable to reproduce the normalisation of the experimental data. The NLO QCD calculations, using various available photon and proton PDFs, describe the measured distributions both in normalisation and shape over the whole E_T^{jet} and η^{jet} range within the experimental and theoretical uncertainties. For $E_T^{jet} \geq 21 \text{ GeV}$, the hadronisation corrections to the NLO QCD calculations only slightly improve the agreement with the data, whereas for $5 \leq E_T^{jet} < 21 \text{ GeV}$, good agreement can only be obtained with the hadronisation corrections. The current precision of the experimental results as well as of the theoretical predictions does not allow one to discriminate between the different photon and proton PDFs using these data alone. However, the information obtained from these measurements could be used to constrain the photon and proton PDFs in global fits of experimental results.

To compare with previous measurements at HERA and at $p\bar{p}$ colliders, the inclusive E_T^{jet} differential cross section was also measured for jets defined using the cone algorithm with $R = 1$. The shape of the γp scaled cross section $S(x_T)$, as a function of the dimensionless variable $x_T = 2E_T^{jet}/W_{\gamma p}$ at $W_{\gamma p} = 200 \text{ GeV}$ for $|\eta^*| < 0.5$, is compatible with that of similar $p\bar{p}$ measurements for $x_T \lesssim 0.2$. The shapes for γp and $p\bar{p}$ are different at larger x_T , where resolved photon structure at large x_γ and direct photon interactions become important.

Acknowledgements

We are grateful to the HERA machine group whose outstanding efforts have made this experiment possible. We thank the engineers and technicians for their work in constructing and now maintaining the H1 detector, our funding agencies for financial support, the DESY technical staff for continual assistance and the DESY directorate for support and for the hospitality which they extend to the non DESY members of the collaboration. We wish to thank M. Fontannaz for valuable discussions and S. Frixione and G. Ridolfi for making their theoretical calculations available to us.

References

- [1] T. Ahmed *et al.* [H1 Collaboration], Phys. Lett. **B 297** (1992) 205.
- [2] M. Derrick *et al.* [ZEUS Collaboration], Phys. Lett. **B 297** (1992) 404.
- [3] S. Catani *et al.*, Phys. Lett. **B 269** (1991) 432.
- [4] C. Albajar *et al.* [UA1 Collaboration], Nucl. Phys. **B 309** (1988) 405.
- [5] G. Arnison *et al.* [UA1 Collaboration], Phys. Lett. **B 172** (1986) 461.
- [6] B. Abbott *et al.* [D0 Collaboration], Phys. Rev. Lett. **86** (2001) 2523 [hep-ex/0008072].
- [7] B. Abbott *et al.* [D0 Collaboration], Phys. Rev. Lett. **82** (1999) 2451 [hep-ex/9807018].
- [8] T. Akesson *et al.* [AFS Collaboration], Phys. Lett. **B 118** (1982) 185;
M. Banner *et al.* [UA2 Collaboration], Phys. Lett. **B 118** (1982) 203;
G. Arnison *et al.* [UA1 Collaboration], Phys. Lett. **B 123** (1983) 115;
T. Akesson *et al.* [AFS Collaboration], Phys. Lett. **B 123** (1983) 133;
P. Bagnaia *et al.* [UA2 Collaboration], Z. Phys. **C 20** (1983) 117;
G. Arnison *et al.* [UA1 Collaboration], Phys. Lett. **B 132** (1983) 214;
P. Bagnaia *et al.* [UA2 Collaboration], Phys. Lett. **B 138** (1984) 430;
J. A. Appel *et al.* [UA2 Collaboration], Phys. Lett. **B 160** (1985) 349;
J. Alitti *et al.* [UA2 Collaboration], Phys. Lett. **B 257** (1991) 232;
F. Abe *et al.* [CDF Collaboration], Phys. Rev. Lett. **62** (1989) 613;
F. Abe *et al.* [CDF Collaboration], Phys. Rev. Lett. **68** (1992) 1104;
F. Abe *et al.* [CDF Collaboration], Phys. Rev. Lett. **70** (1993) 1376;
F. Abe *et al.* [CDF Collaboration], Phys. Rev. Lett. **77** (1996) 438 [hep-ex/9601008];
B. Abbott *et al.* [D0 Collaboration], Phys. Rev. Lett. **86** (2001) 1707 [hep-ex/0011036];
T. Affolder *et al.* [CDF Collaboration], Phys. Rev. **D 64** (2001) 032001 [Erratum-ibid. **D 65** (2002) 039903] [hep-ph/0102074];
V. M. Abazov *et al.* [D0 Collaboration], Phys. Lett. **B 525** (2002) 211 [hep-ex/0109041].
- [9] I. Abt *et al.* [H1 Collaboration], Phys. Lett. **B 314** (1993) 436.
- [10] M. Derrick *et al.* [ZEUS Collaboration], Phys. Lett. **B 342** (1995) 417.
- [11] S. Aid *et al.* [H1 Collaboration], Z. Phys. **C 70** (1996) 17 [hep-ex/9511012].
- [12] J. Breitweg *et al.* [ZEUS Collaboration], Eur. Phys. J. **C 4** (1998) 591 [hep-ex/9802012].
- [13] S. Chekanov *et al.* [ZEUS Collaboration], DESY 02-228 (2002), submitted to Phys. Lett. [hep-ex/0212064].
- [14] S. D. Ellis and D. E. Soper, Phys. Rev. **D 48** (1993) 3160 [hep-ph/9305266].
- [15] S. Catani, Y. L. Dokshitzer, M. H. Seymour and B. R. Webber, Nucl. Phys. **B 406** (1993) 187.
- [16] C. Adloff *et al.* [H1 Collaboration], Nucl. Phys. **B 545** (1999) 3 [hep-ex/9901010].

- [17] C. Adloff *et al.* [H1 Collaboration], Eur. Phys. J. **C 25** (2002) 13 [hep-ex/0201006].
- [18] J. Huth *et al.*, Proceedings of the Summer Study on High Energy Physics, Snowmass, Colorado (1990) 134.
- [19] L. A. del Pozo, PhD Thesis, University of Cambridge, Cambridge (1993) RALT-002.
- [20] C. Adloff *et al.* [H1 Collaboration], Eur. Phys. J. **C 19** (2001) 289 [hep-ex/0010054].
- [21] H. L. Lai *et al.* [CTEQ Collaboration], Eur. Phys. J. **C 12** (2000) 375 [hep-ph/9903282].
- [22] A. D. Martin, R. G. Roberts, W. J. Stirling and R. S. Thorne, Eur. Phys. J. **C 14** (2000) 133 [hep-ph/9907231].
- [23] M. Glück, E. Reya and A. Vogt, Z. Phys. **C 67** (1995) 433.
- [24] J. Breitweg *et al.* [ZEUS Collaboration], Phys. Lett. **B 487** (2000) 53 [hep-ex/0005018].
- [25] C. Adloff *et al.* [H1 Collaboration], Eur. Phys. J. **C 21** (2001) 33 [hep-ex/0012053].
- [26] J. Pumplin *et al.*, JHEP **0207** (2002) 012 [hep-ph/0201195].
- [27] S. Chekanov *et al.* [ZEUS Collaboration], Eur. Phys. J. **C 23** (2002) 615 [hep-ex/0112029].
- [28] M. Glück, E. Reya and A. Vogt, Phys. Rev. **D 46** (1992) 1973.
- [29] M. Glück, E. Reya and A. Vogt, Phys. Rev. **D 45** (1992) 3986.
- [30] P. Aurenche, J. P. Guillet and M. Fontannaz, Z. Phys. **C 64** (1994) 621 [hep-ph/9406382].
- [31] For a review, see: M. Krawczyk *et al.*, Phys. Rept. **345** (2001) 265 [hep-ph/0011083].
- [32] C. Adloff *et al.* [H1 Collaboration], Phys. Lett. **B 483** (2000) 36 [hep-ex/0003011].
- [33] S. Frixione and G. Ridolfi, Nucl. Phys. **B 507** (1997) 315 [hep-ph/9707345].
- [34] P. Kessler, Il Nuovo Cimento **17** (1960) 809;
V. M. Budnev *et al.*, Phys. Rept. **15** (1974) 181;
S. Frixione *et al.*, Phys. Lett. **B 319** (1993) 339 [hep-ph/9310350].
- [35] E. Witten, Nucl. Phys. **B 120** (1977) 189.
- [36] M. Klasen and G. Kramer, Z. Phys. **C 76** (1997) 67 [hep-ph/9611450].
- [37] B. W. Harris and J. F. Owens, Phys. Rev. **D 56** (1997) 4007 [hep-ph/9704324].
- [38] P. Aurenche *et al.*, Eur. Phys. J. **C 17** (2000) 413 [hep-ph/0006011].
- [39] S. Frixione, Nucl. Phys. **B 507** (1997) 295 [hep-ph/9706545].
- [40] S. Ferron, PhD Thesis, École polytechnique, Palaiseau (2001) unpublished, available from http://www-h1.desy.de/publications/theses_list.html.

- [41] T. Sjöstrand, Comp. Phys. Commun. **82** (1994) 74;
T. Sjöstrand *et al.*, Comp. Phys. Commun. **135** (2001) 74.
- [42] G. Marchesini *et al.*, Comp. Phys. Commun. **67** (1992) 465.
- [43] R. Engel, Z. Phys. **C 66** (1995) 203;
R. Engel and J. Ranft, Phys. Rev. **D 54** (1996) 4244.
- [44] R. Brun *et al.*, GEANT3 User's Guide, CERN-DD/EE/84-1.
- [45] B. Andersson *et al.*, Phys. Rept. **97** (1983) 31.
- [46] T. Sjöstrand, Comp. Phys. Commun. **39** (1986) 347;
T. Sjöstrand and M. Bengtsson, Comp. Phys. Commun. **43** (1987) 367.
- [47] B. R. Webber, Nucl. Phys. **B 238** (1984) 192.
- [48] A. Capella *et al.*, Phys. Rept. **236** (1994) 225.
- [49] I. Abt *et al.* [H1 Collaboration], Nucl. Instrum. Meth. **A 386** (1997) 310 and 348.
- [50] B. Andrieu *et al.*, Nucl. Instrum. Meth. **A 336** (1993) 460.
- [51] R. D. Appuhn *et al.*, Nucl. Instrum. Meth. **A 386** (1997) 397.
- [52] C. Adloff *et al.* [H1 Collaboration], Z. Phys. **C 74** (1997) 221 [hep-ex/9702003].
- [53] A. Blondel and F. Jacquet, Proceedings of the Study of an *ep* Facility for Europe, ed. U. Amaldi, DESY 79-48 (1979) 391.
- [54] C. Adloff *et al.* [H1 Collaboration], Eur. Phys. J. **C 17** (2000) 567 [hep-ex/0007035].
- [55] G. A. Schuler and H. Spiesberger, Proceedings of the Workshop “*Physics at HERA*”, vol. 3, eds. W. Buchmüller, G. Ingelman, DESY (1992) 1419.
- [56] C. Adloff *et al.* [H1 Collaboration], Eur. Phys. J. **C 10** (1999) 363 [hep-ex/9810020].
- [57] R. Hagedorn, Riv. Nuovo Cim. **6:10** (1983) 1.

E_T^{jet} range [GeV]	$d\sigma/dE_T^{jet}$ [pb/GeV]	$\Delta_{stat.}$	$\Delta_{syst.}$	$\Delta_{e.s.}$	$(1 + \delta_{frag.})$	$(1 + \delta_{u.e.})$	$(1 + \delta_{had.})$
$95 \leq W_{\gamma p} \leq 285$ GeV							
21 ... 28	65.4	± 0.6	± 1.6	$^{+5.5}_{-5.3}$	0.95 ± 0.02	1.08 ± 0.01	1.03 ± 0.03
28 ... 35	14.0	± 0.3	± 0.3	$^{+1.4}_{-1.2}$	0.95 ± 0.02	1.06 ± 0.02	1.00 ± 0.04
35 ... 42	3.56	± 0.14	± 0.09	$^{+0.39}_{-0.33}$	0.95 ± 0.01	1.04 ± 0.01	1.00 ± 0.02
42 ... 52	0.908	± 0.060	± 0.018	$^{+0.107}_{-0.095}$	0.95 ± 0.01	1.01 ± 0.02	0.96 ± 0.01
52 ... 62	0.192	± 0.028	± 0.012	$^{+0.023}_{-0.021}$	0.97 ± 0.03	1.01 ± 0.03	0.98 ± 0.04
62 ... 75	0.0483	± 0.0121	± 0.0018	$^{+0.0063}_{-0.0071}$	0.96 ± 0.04	1.00 ± 0.05	0.96 ± 0.04
$95 \leq W_{\gamma p} < 212$ GeV							
21 ... 28	32.7	± 0.4	± 0.7	$^{+2.6}_{-3.0}$	0.94 ± 0.02	1.07 ± 0.01	1.00 ± 0.03
28 ... 35	6.21	± 0.19	± 0.18	$^{+0.60}_{-0.50}$	0.94 ± 0.01	1.04 ± 0.01	0.98 ± 0.02
35 ... 42	1.51	± 0.09	± 0.03	$^{+0.15}_{-0.14}$	0.94 ± 0.02	1.04 ± 0.01	0.98 ± 0.01
42 ... 52	0.236	± 0.030	± 0.008	$^{+0.025}_{-0.024}$	0.93 ± 0.02	1.00 ± 0.03	0.93 ± 0.02
52 ... 62	0.0360	± 0.0115	± 0.0009	$^{+0.0052}_{-0.0041}$	0.92 ± 0.04	1.00 ± 0.05	0.92 ± 0.04
62 ... 75	0.00511	± 0.00365	± 0.00019	$^{+0.00041}_{-0.00115}$	0.90 ± 0.11	0.98 ± 0.12	0.88 ± 0.10
$212 \leq W_{\gamma p} \leq 285$ GeV							
21 ... 28	32.8	± 0.4	± 1.0	$^{+2.8}_{-2.3}$	0.97 ± 0.01	1.10 ± 0.02	1.06 ± 0.03
28 ... 35	7.81	± 0.21	± 0.21	$^{+0.83}_{-0.71}$	0.95 ± 0.02	1.07 ± 0.03	1.03 ± 0.06
35 ... 42	2.05	± 0.11	± 0.07	$^{+0.23}_{-0.20}$	0.96 ± 0.01	1.05 ± 0.03	1.01 ± 0.03
42 ... 52	0.676	± 0.053	± 0.017	$^{+0.083}_{-0.071}$	0.97 ± 0.02	1.01 ± 0.02	0.98 ± 0.02
52 ... 62	0.157	± 0.026	± 0.012	$^{+0.018}_{-0.017}$	0.99 ± 0.03	1.01 ± 0.04	1.00 ± 0.05
62 ... 75	0.0434	± 0.0117	± 0.0018	$^{+0.0061}_{-0.0057}$	0.97 ± 0.04	1.00 ± 0.05	0.97 ± 0.05

Table 1: Measured differential e^+p cross section $d\sigma/dE_T^{jet}$ for inclusive jet photoproduction ($Q^2 \leq 1$ GeV²), integrated over $-1 \leq \eta^{jet} \leq 2.5$ in three regions of $W_{\gamma p}$. Jets are defined using the inclusive k_\perp algorithm. The statistical ($\Delta_{stat.}$), systematic ($\Delta_{syst.}$) (excluding LAr energy scale) and LAr energy scale ($\Delta_{e.s.}$) uncertainties are shown separately. The correction factors applied to the NLO QCD predictions are also shown separately as $(1 + \delta_{frag.})$, for fragmentation, $(1 + \delta_{u.e.})$, for the underlying event, and the product $(1 + \delta_{had.})$ for the total hadronisation correction.

E_T^{jet} range [GeV]	$d\sigma/dE_T^{jet}$ [pb/GeV]	$\Delta_{stat.}$	$\Delta_{syst.}$	$\Delta_{e.s.}$	$(1 + \delta_{frag.})$	$(1 + \delta_{u.e.})$	$(1 + \delta_{hadr.})$
$164 \leq W_{\gamma p} \leq 242 \text{ GeV} ; Q^2 \leq 0.01 \text{ GeV}^2$							
5...8	24600	± 200	± 1600	$^{+3000}_{-2900}$	0.72 ± 0.06	1.77 ± 0.23	1.25 ± 0.06
8...12	3070	± 60	± 230	$^{+520}_{-470}$	0.80 ± 0.08	1.66 ± 0.11	1.31 ± 0.06
12...16	505	± 26	± 30	$^{+94}_{-84}$	0.87 ± 0.08	1.43 ± 0.10	1.23 ± 0.04
16...21	126	± 11	± 6	$^{+27}_{-19}$	0.83 ± 0.11	1.26 ± 0.09	1.04 ± 0.09
21...28	28.3	± 6.1	± 4.6	$^{+10.1}_{-6.9}$	0.86 ± 0.17	1.23 ± 0.13	1.05 ± 0.17
$164 \leq W_{\gamma p} \leq 242 \text{ GeV} ; Q^2 \leq 1 \text{ GeV}^2$							
21...28	30.1	± 0.4	± 0.8	$^{+2.4}_{-2.5}$	0.95 ± 0.02	1.09 ± 0.01	1.04 ± 0.03
28...35	6.74	± 0.19	± 0.18	$^{+0.63}_{-0.58}$	0.95 ± 0.01	1.07 ± 0.02	1.01 ± 0.04
35...42	1.66	± 0.10	± 0.04	$^{+0.18}_{-0.14}$	0.96 ± 0.01	1.04 ± 0.02	1.00 ± 0.02
42...52	0.417	± 0.041	± 0.013	$^{+0.043}_{-0.040}$	0.96 ± 0.02	1.01 ± 0.03	0.97 ± 0.02
52...62	0.0773	± 0.0174	± 0.0066	$^{+0.0113}_{-0.0119}$	0.95 ± 0.03	1.00 ± 0.04	0.95 ± 0.03
62...75	0.0132	± 0.0059	± 0.0014	$^{+0.0016}_{-0.0019}$	0.94 ± 0.07	0.95 ± 0.08	0.89 ± 0.09

Table 2: Measured differential e^+p cross section $d\sigma/dE_T^{jet}$ for inclusive jet photoproduction, integrated over $-1 \leq \eta^{jet} \leq 2.5$ in the kinematic region $164 \leq W_{\gamma p} \leq 242 \text{ GeV}$ (see Tab. 1 caption for further details).

η^{jet} range	$d\sigma/d\eta^{jet}$ [pb]	$\Delta_{stat.}$	$\Delta_{syst.}$	$\Delta_{e.s.}$	$(1 + \delta_{frag.})$	$(1 + \delta_{u.e.})$	$(1 + \delta_{hadr.})$
$21 \leq E_T^{jet} \leq 75$ GeV							
-1...0	37.8	± 1.2	± 2.1	$^{+3.0}_{-2.5}$	0.84 ± 0.03	1.04 ± 0.03	0.87 ± 0.05
0...0.5	173	± 4	± 4	$^{+12}_{-12}$	0.90 ± 0.03	1.06 ± 0.02	0.96 ± 0.05
0.5...1	257	± 5	± 7	$^{+21}_{-23}$	0.94 ± 0.02	1.06 ± 0.02	1.00 ± 0.04
1...1.5	253	± 4	± 6	$^{+25}_{-20}$	0.96 ± 0.01	1.07 ± 0.02	1.02 ± 0.03
1.5...2	237	± 4	± 7	$^{+22}_{-19}$	0.99 ± 0.01	1.09 ± 0.01	1.08 ± 0.01
2...2.5	186	± 4	± 4	$^{+17}_{-19}$	1.01 ± 0.01	1.11 ± 0.02	1.12 ± 0.01
$21 \leq E_T^{jet} < 35$ GeV							
-1...0	37.6	± 1.1	± 2.1	$^{+2.9}_{-2.5}$	0.84 ± 0.03	1.04 ± 0.03	0.87 ± 0.05
0...0.5	166	± 4	± 4	$^{+11}_{-11}$	0.90 ± 0.03	1.06 ± 0.02	0.96 ± 0.05
0.5...1	241	± 4	± 6	$^{+19}_{-21}$	0.94 ± 0.02	1.07 ± 0.02	1.00 ± 0.04
1...1.5	233	± 4	± 6	$^{+23}_{-18}$	0.96 ± 0.02	1.07 ± 0.02	1.02 ± 0.03
1.5...2	220	± 4	± 7	$^{+20}_{-18}$	0.99 ± 0.01	1.10 ± 0.01	1.09 ± 0.01
2...2.5	174	± 4	± 4	$^{+16}_{-18}$	1.01 ± 0.01	1.11 ± 0.02	1.13 ± 0.02
$35 \leq E_T^{jet} < 52$ GeV							
0...0.5	7.56	± 0.75	± 0.64	$^{+1.08}_{-0.76}$	0.87 ± 0.03	1.01 ± 0.02	0.87 ± 0.03
0.5...1	14.8	± 1.1	± 0.4	$^{+1.5}_{-1.4}$	0.94 ± 0.02	1.03 ± 0.02	0.96 ± 0.03
1...1.5	18.3	± 1.2	± 0.4	$^{+1.8}_{-1.6}$	0.96 ± 0.01	1.03 ± 0.02	0.99 ± 0.02
1.5...2	15.1	± 1.1	± 0.3	$^{+1.6}_{-1.4}$	0.98 ± 0.01	1.04 ± 0.02	1.02 ± 0.01
2...2.5	11.5	± 1.0	± 0.2	$^{+1.5}_{-1.3}$	0.99 ± 0.02	1.06 ± 0.02	1.05 ± 0.02
$52 \leq E_T^{jet} \leq 75$ GeV							
0.5...1	1.16	± 0.33	± 0.08	$^{+0.08}_{-0.11}$	0.93 ± 0.05	1.03 ± 0.05	0.96 ± 0.05
1...1.5	1.69	± 0.37	± 0.10	$^{+0.21}_{-0.23}$	0.97 ± 0.04	0.97 ± 0.05	0.94 ± 0.06
1.5...2	1.84	± 0.39	± 0.12	$^{+0.25}_{-0.19}$	0.99 ± 0.04	1.03 ± 0.04	1.02 ± 0.04
2...2.5	0.458	± 0.189	± 0.040	$^{+0.077}_{-0.069}$	0.98 ± 0.06	1.04 ± 0.07	1.02 ± 0.08

Table 3: Measured differential e^+p cross section $d\sigma/d\eta^{jet}$ for inclusive jet photoproduction ($Q^2 \leq 1$ GeV²), integrated over four E_T^{jet} ranges in the kinematic region $95 \leq W_{\gamma p} \leq 285$ GeV (see Tab. 1 caption for further details).

η^{jet} range	$d\sigma/d\eta^{jet}$	$\Delta_{stat.}$	$\Delta_{syst.}$	$\Delta_{e.s.}$	$(1 + \delta_{frag.})$	$(1 + \delta_{u.e.})$	$(1 + \delta_{hadr.})$
$21 \leq E_T^{jet} < 35 \text{ GeV} \quad ; \quad 95 \leq W_{\gamma p} < 212 \text{ GeV}$							
0...0.5	32.6	± 1.5	± 0.9	$^{+1.7}_{-3.2}$	0.79 ± 0.04	1.02 ± 0.04	0.81 ± 0.06
0.5...1	114	± 3	± 4	$^{+10}_{-9}$	0.90 ± 0.02	1.06 ± 0.02	0.95 ± 0.03
1...1.5	141	± 3	± 3	$^{+12}_{-12}$	0.93 ± 0.02	1.05 ± 0.02	0.98 ± 0.04
1.5...2	142	± 3	± 5	$^{+13}_{-11}$	0.98 ± 0.01	1.06 ± 0.02	1.04 ± 0.02
2...2.5	114	± 3	± 3	$^{+9}_{-14}$	0.99 ± 0.02	1.10 ± 0.03	1.09 ± 0.02
$21 \leq E_T^{jet} < 35 \text{ GeV} \quad ; \quad 212 \leq W_{\gamma p} \leq 285 \text{ GeV}$							
-1...0	37.3	± 1.2	± 1.9	$^{+3.1}_{-2.9}$	0.85 ± 0.03	1.04 ± 0.03	0.88 ± 0.05
0...0.5	133	± 3	± 4	$^{+9}_{-8}$	0.94 ± 0.03	1.07 ± 0.02	1.01 ± 0.05
0.5...1	127	± 3	± 6	$^{+9}_{-12}$	0.97 ± 0.02	1.08 ± 0.04	1.05 ± 0.05
1...1.5	91.7	± 2.6	± 3.7	$^{+11.6}_{-6.2}$	1.01 ± 0.02	1.10 ± 0.03	1.11 ± 0.03
1.5...2	78.7	± 2.6	± 2.2	$^{+6.8}_{-6.3}$	1.02 ± 0.02	1.16 ± 0.03	1.19 ± 0.03
2...2.5	59.6	± 2.3	± 2.4	$^{+7.4}_{-3.9}$	1.05 ± 0.03	1.14 ± 0.03	1.20 ± 0.03
$35 \leq E_T^{jet} < 52 \text{ GeV} \quad ; \quad 95 \leq W_{\gamma p} < 212 \text{ GeV}$							
0.5...1	2.72	± 0.46	± 0.17	$^{+0.16}_{-0.18}$	0.82 ± 0.04	1.03 ± 0.04	0.85 ± 0.05
1...1.5	8.07	± 0.81	± 0.19	$^{+0.76}_{-0.72}$	0.93 ± 0.02	1.02 ± 0.02	0.95 ± 0.02
1.5...2	8.27	± 0.81	± 0.20	$^{+0.87}_{-0.75}$	0.96 ± 0.02	1.02 ± 0.02	0.98 ± 0.02
2...2.5	6.57	± 0.71	± 0.19	$^{+0.84}_{-0.71}$	0.97 ± 0.03	1.05 ± 0.03	1.02 ± 0.02
$35 \leq E_T^{jet} < 52 \text{ GeV} \quad ; \quad 212 \leq W_{\gamma p} \leq 285 \text{ GeV}$							
0...0.5	7.44	± 0.75	± 0.62	$^{+1.04}_{-0.72}$	0.87 ± 0.03	1.01 ± 0.02	0.88 ± 0.03
0.5...1	12.1	± 1.0	± 0.4	$^{+1.3}_{-1.2}$	0.96 ± 0.02	1.03 ± 0.02	0.99 ± 0.03
1...1.5	10.2	± 0.9	± 0.2	$^{+1.0}_{-0.9}$	0.99 ± 0.02	1.04 ± 0.02	1.02 ± 0.03
1.5...2	6.85	± 0.77	± 0.19	$^{+0.77}_{-0.71}$	1.00 ± 0.02	1.07 ± 0.02	1.08 ± 0.02
2...2.5	4.97	± 0.63	± 0.13	$^{+0.62}_{-0.56}$	1.02 ± 0.03	1.07 ± 0.04	1.09 ± 0.03
$52 \leq E_T^{jet} \leq 75 \text{ GeV} \quad ; \quad 212 \leq W_{\gamma p} \leq 285 \text{ GeV}$							
0.5...1	1.17	± 0.33	± 0.08	$^{+0.07}_{-0.11}$	0.94 ± 0.05	1.02 ± 0.05	0.96 ± 0.05
1...1.5	1.49	± 0.35	± 0.08	$^{+0.17}_{-0.18}$	0.99 ± 0.04	0.96 ± 0.06	0.96 ± 0.07
1.5...2	1.24	± 0.32	± 0.12	$^{+0.19}_{-0.15}$	1.03 ± 0.06	1.02 ± 0.05	1.05 ± 0.07
2...2.5	0.423	± 0.191	± 0.045	$^{+0.073}_{-0.058}$	1.02 ± 0.08	1.15 ± 0.18	1.17 ± 0.18

Table 4: Measured differential e^+p cross section $d\sigma/d\eta^{jet}$ for inclusive jet photoproduction ($Q^2 \leq 1 \text{ GeV}^2$). The phase space of the measurement is divided into two regions of $W_{\gamma p}$ and three regions of E_T^{jet} (see Tab. 1 caption for further details).

η^{jet} range	$d\sigma/d\eta^{jet}$	$\Delta_{stat.}$	$\Delta_{syst.}$	$\Delta_{e.s.}$	$(1 + \delta_{frag.})$	$(1 + \delta_{u.e.})$	$(1 + \delta_{had.})$
		[nb]					
$5 \leq E_T^{jet} < 12$ GeV							
$-1 \dots -0.5$	16.2	± 0.4	± 1.1	$^{+2.0}_{-1.8}$	0.79 ± 0.06	1.29 ± 0.06	1.02 ± 0.03
$-0.5 \dots 0$	18.1	± 0.4	± 1.4	$^{+2.1}_{-2.0}$	0.80 ± 0.06	1.45 ± 0.08	1.15 ± 0.02
$0 \dots 0.5$	20.6	± 0.4	± 1.4	$^{+2.5}_{-2.3}$	0.73 ± 0.06	1.64 ± 0.13	1.19 ± 0.02
$0.5 \dots 1$	24.1	± 0.5	± 1.7	$^{+2.7}_{-2.8}$	0.68 ± 0.06	1.89 ± 0.27	1.27 ± 0.06
$1 \dots 1.5$	25.8	± 0.4	± 1.7	$^{+3.1}_{-2.8}$	0.69 ± 0.06	1.99 ± 0.32	1.35 ± 0.10
$12 \leq E_T^{jet} \leq 21$ GeV							
$-0.5 \dots 0$	0.584	± 0.081	± 0.034	$^{+0.063}_{-0.102}$	0.77 ± 0.11	1.12 ± 0.07	0.87 ± 0.11
$0 \dots 0.5$	0.987	± 0.110	± 0.080	$^{+0.106}_{-0.102}$	0.91 ± 0.09	1.22 ± 0.06	1.11 ± 0.11
$0.5 \dots 1$	1.02	± 0.11	± 0.07	$^{+0.09}_{-0.20}$	0.89 ± 0.09	1.33 ± 0.08	1.19 ± 0.09
$1 \dots 1.5$	0.803	± 0.096	± 0.060	$^{+0.175}_{-0.110}$	0.91 ± 0.07	1.53 ± 0.14	1.39 ± 0.08
$1.5 \dots 2$	1.12	± 0.11	± 0.08	$^{+0.26}_{-0.15}$	0.83 ± 0.14	1.74 ± 0.33	1.41 ± 0.08
$2 \dots 2.5$	0.824	± 0.078	± 0.056	$^{+0.264}_{-0.171}$	0.88 ± 0.09	1.75 ± 0.27	1.53 ± 0.14

Table 5: Measured differential e^+p cross section $d\sigma/d\eta^{jet}$ for inclusive jet photoproduction ($Q^2 \leq 0.01$ GeV²), integrated over two E_T^{jet} ranges in the kinematic region $164 \leq W_{\gamma p} \leq 242$ GeV (see Tab. 1 caption for further details).

E_T^{jet} range [GeV]	$\langle E_T^{jet} \rangle$	$d\sigma/dE_T^{jet}$	$\Delta_{stat.}$	$\Delta_{syst.}$	$\Delta_{e.s.}$
$164 \leq W_{\gamma p} \leq 242 \text{ GeV} ; Q^2 \leq 0.01 \text{ GeV}^2$					
5...8	6.1	39900	± 200	± 2600	$^{+4700}_{-4400}$
8...12	9.3	3840	± 60	± 250	$^{+690}_{-570}$
12...16	14.3	595	± 28	± 35	$^{+91}_{-82}$
16...21	18.1	126	± 12	± 7	$^{+33}_{-18}$
$164 \leq W_{\gamma p} \leq 242 \text{ GeV} ; Q^2 \leq 1 \text{ GeV}^2$					
21...28	23.6	31.3	± 0.4	± 0.8	$^{+3.0}_{-2.9}$
28...35	30.8	6.66	± 0.19	± 0.18	$^{+0.56}_{-0.57}$
35...42	37.8	1.73	± 0.10	± 0.06	$^{+0.19}_{-0.16}$
42...52	45.8	0.415	± 0.042	± 0.014	$^{+0.047}_{-0.044}$
52...62	55.8	0.0794	± 0.0179	± 0.0048	$^{+0.0131}_{-0.0100}$
62...75	66.4	0.0143	± 0.0065	± 0.0004	$^{+0.0023}_{-0.0021}$

Table 6: Measured differential e^+p cross section $d\sigma/dE_T^{jet}$ for inclusive jet photoproduction integrated over $-1 \leq \eta^{jet} \leq 2.5$ in the kinematic region $164 \leq W_{\gamma p} \leq 242 \text{ GeV}$. Jets are defined using the cone algorithm with $R = 1$. For each range of E_T^{jet} , the average value of E_T^{jet} calculated with PYTHIA is given in the second column. The statistical ($\Delta_{stat.}$), systematic ($\Delta_{syst.}$) and LAr energy scale ($\Delta_{e.s.}$) uncertainties are shown separately.

x_T	$S(x_T)$	$\Delta_{stat.}$	$\Delta_{syst.}$	$\Delta_{e.s.}$
0.09	0.0441	± 0.0011	± 0.0024	± 0.0078
0.13	0.0201	± 0.0014	± 0.0012	± 0.0028
0.18	0.00658	± 0.00106	± 0.00068	± 0.00241
0.25	0.00236	± 0.00005	± 0.00015	± 0.00022
0.40	0.000684	± 0.000053	± 0.000016	± 0.000073
0.56	0.000185	± 0.000047	± 0.000009	± 0.000028

Table 7: Scaled γp cross section at $W_{\gamma p} = 200 \text{ GeV}$ as a function of x_T for $|\eta^*| \leq 0.5$. Jets are found with the cone algorithm ($R = 1$). The statistical ($\Delta_{stat.}$), systematic ($\Delta_{syst.}$) and LAr energy scale ($\Delta_{e.s.}$) uncertainties are shown separately.

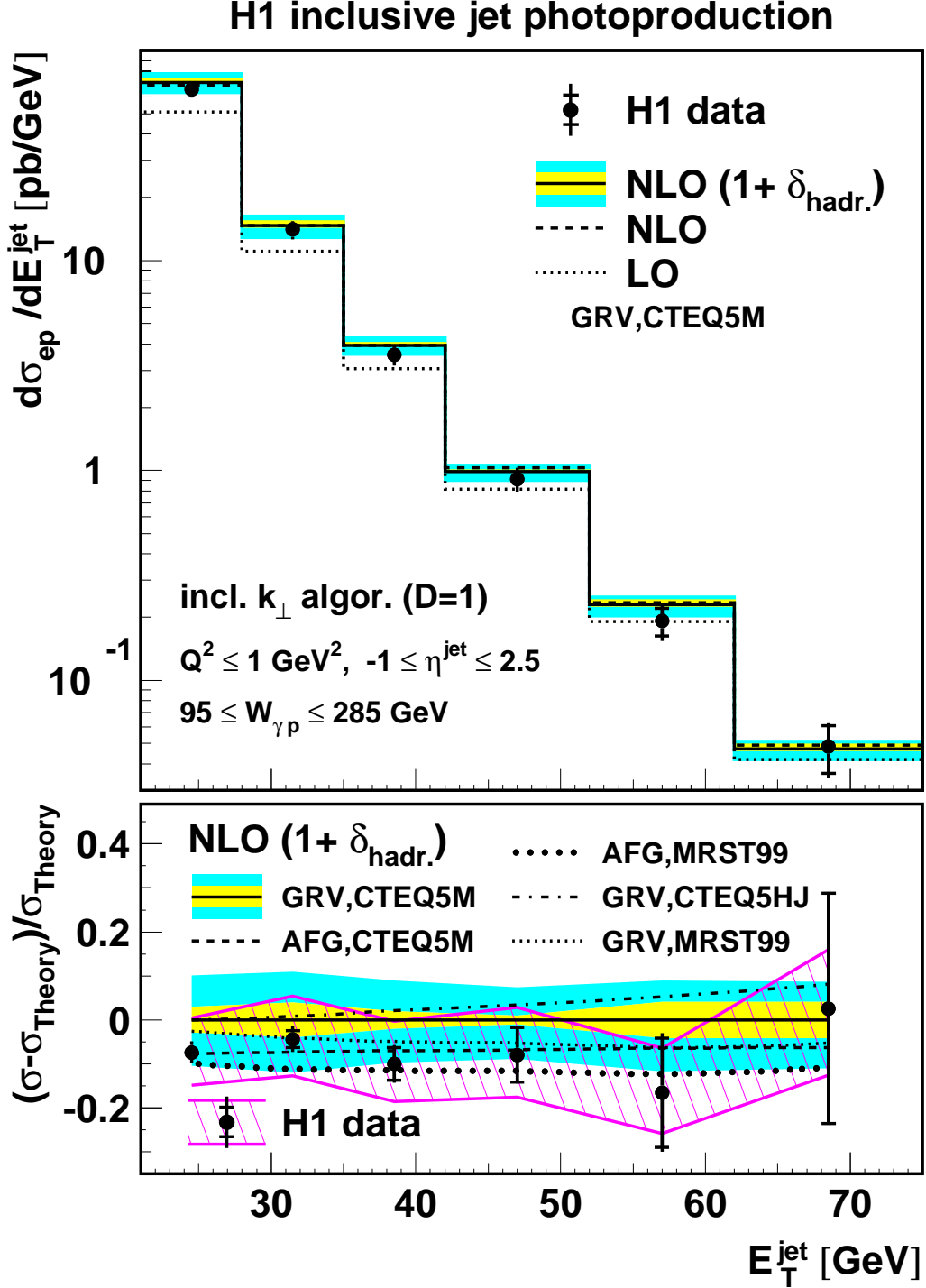


Figure 2: Top: differential e^+p cross section for inclusive jet production as a function of E_T^{jet} integrated over $-1 \leq \eta^{jet} \leq 2.5$. The data are compared with LO and NLO QCD calculations using GRV photon PDFs and CTEQ5M proton PDFs. Bottom: relative difference between the data or different calculations and the NLO prediction with hadronisation corrections. The uncertainty associated with the LAr energy scale is shown as a hatched band. The shaded band displays the uncertainty on the NLO QCD predictions. The inside part shows the uncertainty associated with the hadronisation corrections, the outside part shows the uncertainty associated with the choice of the renormalisation and factorisation scales and both uncertainties are added linearly.

H1 inclusive jet photoproduction

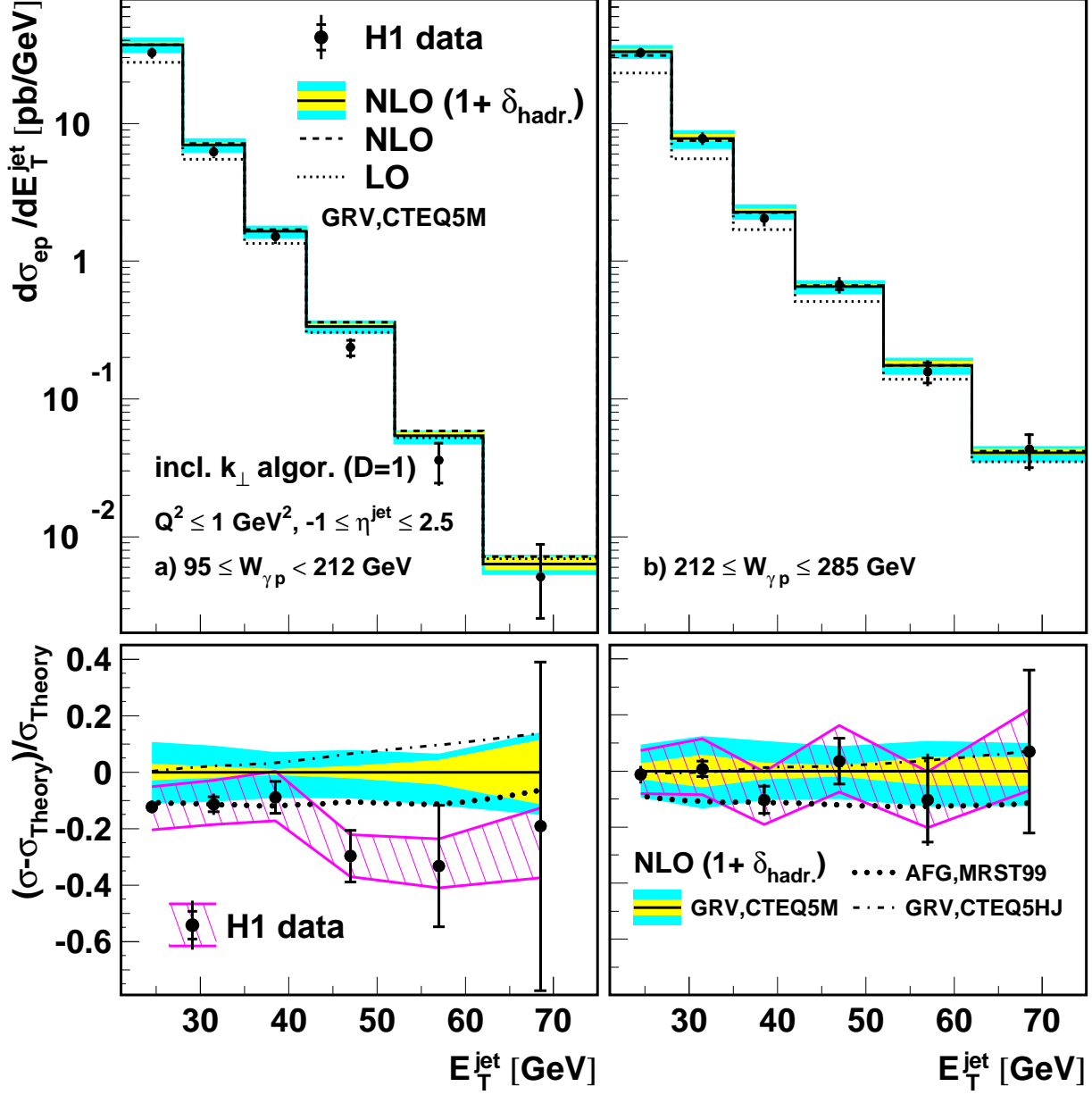


Figure 3: Top: differential e^+p cross section for inclusive jet production as a function of E_T^{jet} integrated over $-1 \leq \eta^{\text{jet}} \leq 2.5$ for $95 \leq W_{\gamma p} < 212$ GeV (a) and $212 \leq W_{\gamma p} \leq 285$ GeV (b). Bottom: relative difference between the data or different calculations and the NLO calculation, including hadronisation corrections, based on GRV and CTEQ5M (see Fig. 2 caption for further details).

H1 inclusive jet photoproduction

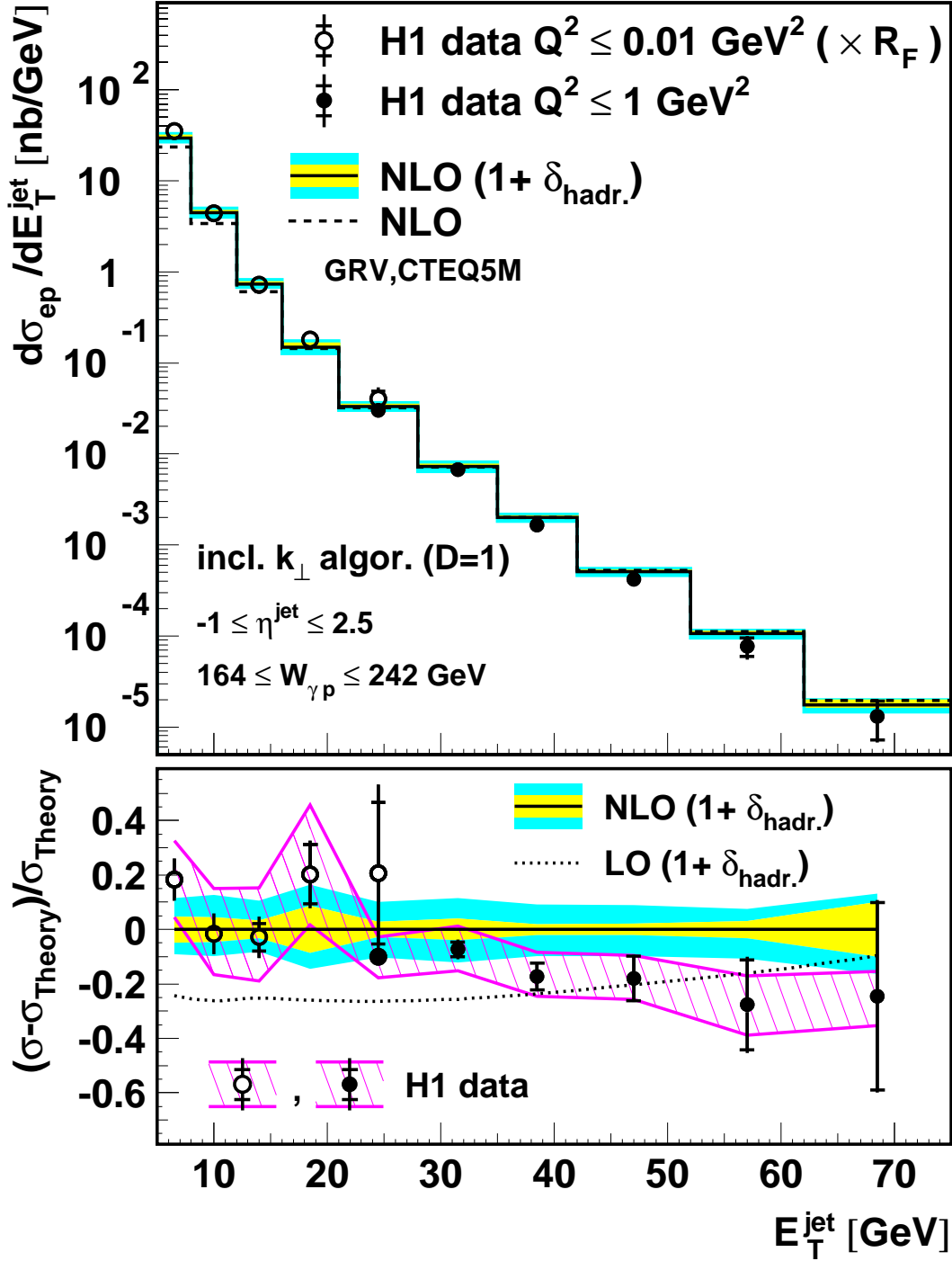


Figure 4: Top: differential e^+p cross section for inclusive jet production as a function of E_T^{jet} integrated over $-1 \leq \eta^{jet} \leq 2.5$ and $Q^2 \leq 1 \text{ GeV}^2$. The “low” E_T^{jet} part, measured for $Q^2 \leq 0.01 \text{ GeV}^2$, is corrected by a factor R_F which is the ratio of the photon fluxes in the two Q^2 regions (see text). The photon-proton centre-of-mass energy is restricted to the range $164 \leq W_{\gamma p} \leq 242 \text{ GeV}$. The data stemming from the analysis at “low” and “high” E_T^{jet} are indicated by empty and full points respectively. Bottom: relative difference between the data or LO QCD prediction and the NLO calculation, including hadronisation corrections, based on GRV and CTEQ5M (see Fig. 2 caption for further details).

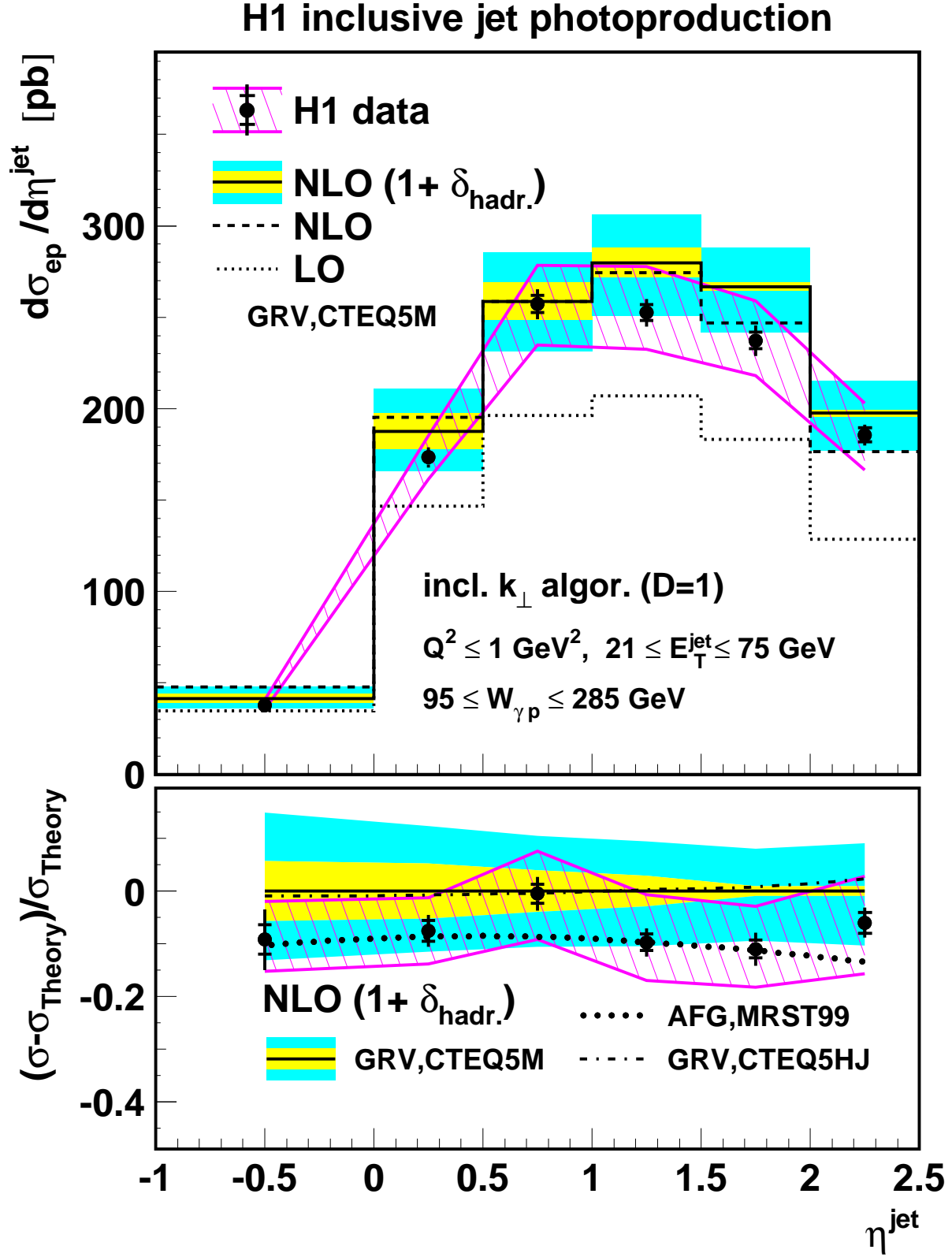


Figure 5: Top: differential e^+p cross section for inclusive jet production as a function of η^{jet} integrated over $21 \leq E_T^{\text{jet}} \leq 75 \text{ GeV}$. Bottom: relative difference between the data or different calculations and the NLO calculation, including hadronisation corrections, based on GRV and CTEQ5M (see Fig. 2 caption for further details).

H1 inclusive jet photoproduction

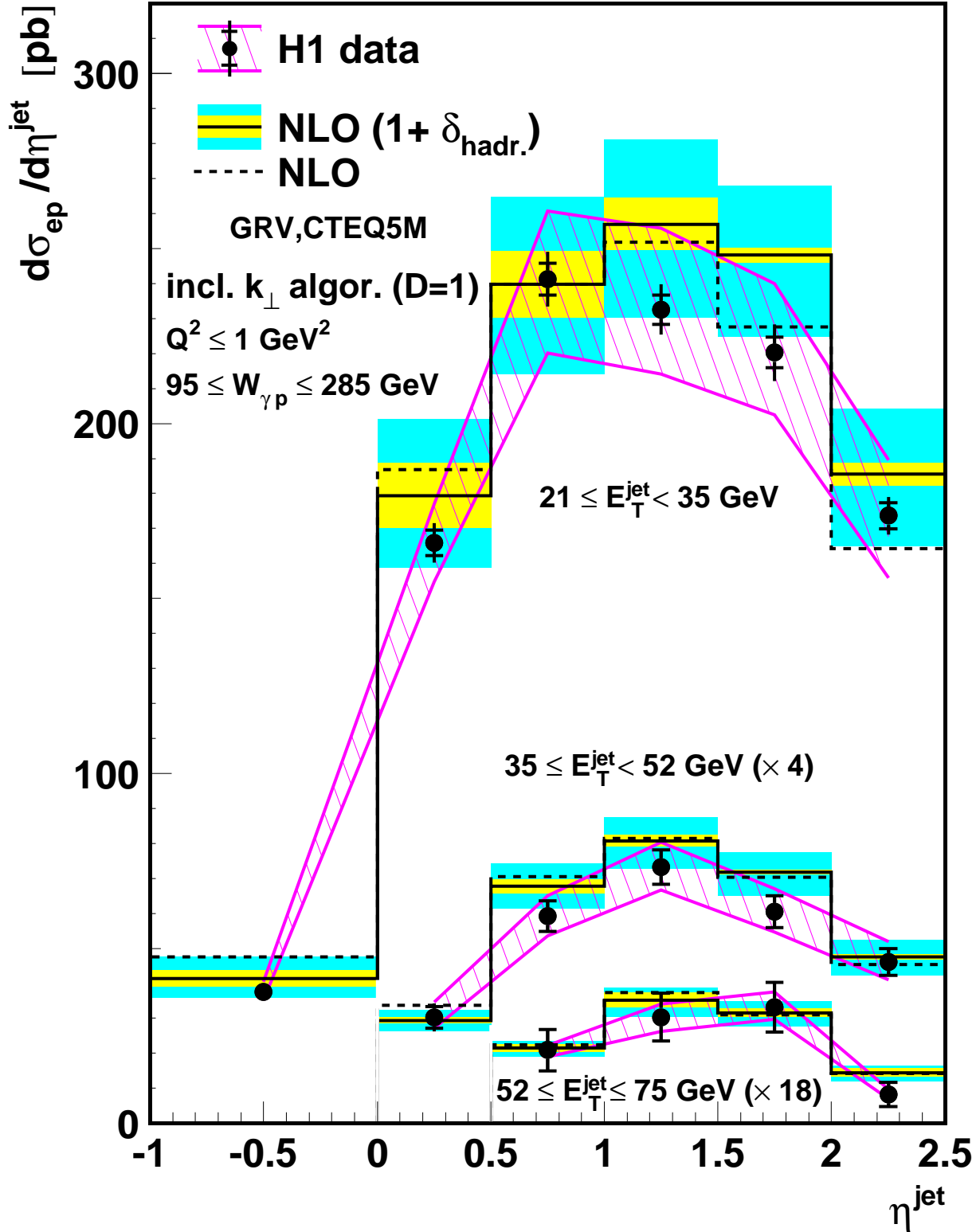


Figure 6: Differential e^+p cross section for inclusive jet production as a function of η^{jet} integrated over various E_T^{jet} ranges. The data are compared with NLO QCD predictions obtained by using GRV photon PDFs and CTEQ5M proton PDFs (see Fig. 2 caption for further details).

H1 inclusive jet photoproduction

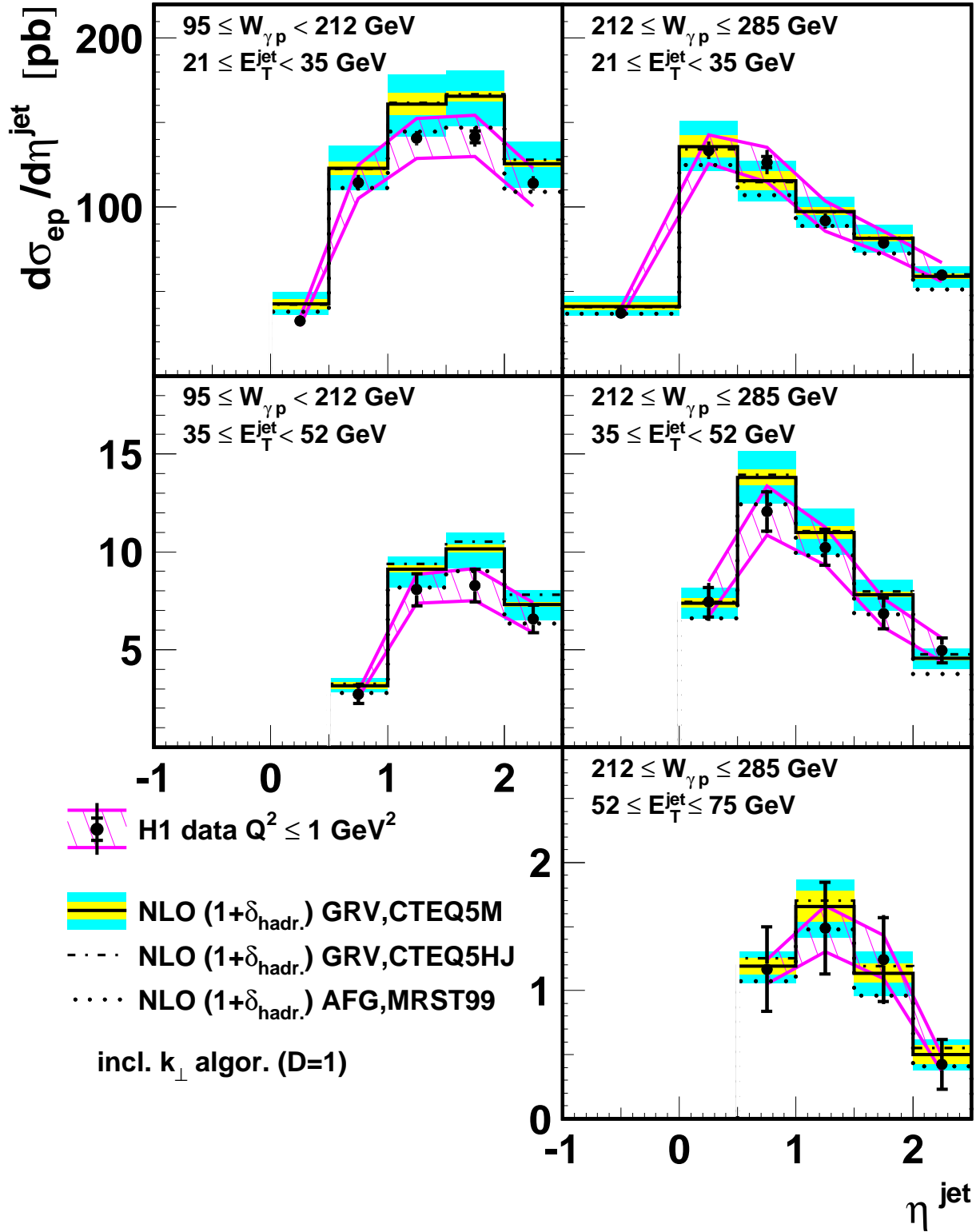


Figure 7: Differential e^+p cross section for inclusive jet production as a function of η^{jet} integrated over various E_T^{jet} and $W_{\gamma p}$ ranges. The data are compared with NLO QCD predictions obtained by using different photon and proton PDFs (see Fig. 2 caption for further details).

H1 inclusive jet photoproduction

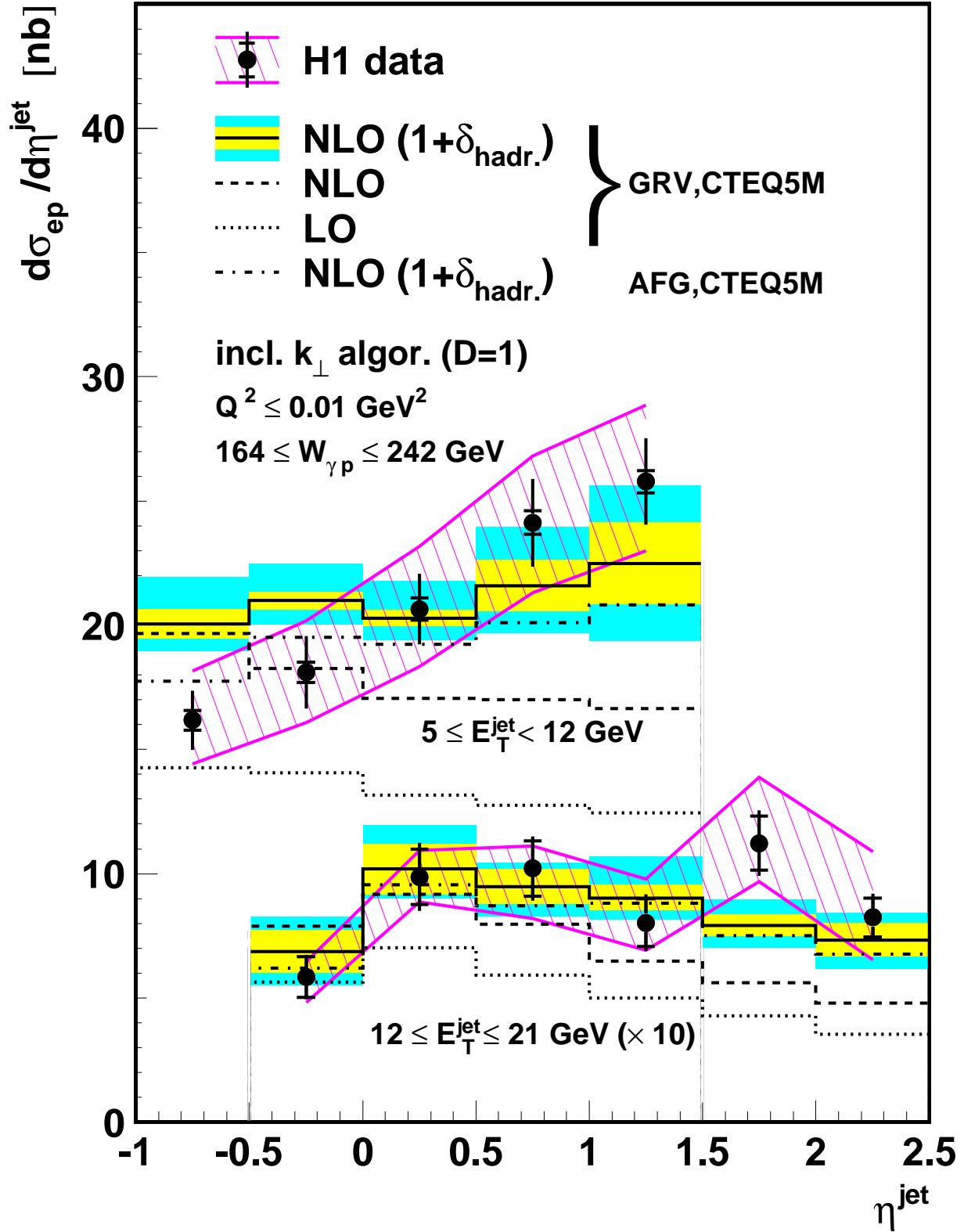


Figure 8: Differential e^+p cross section for inclusive jet production as a function of η^{jet} integrated over various E_T^{jet} ranges. The data are compared with LO and NLO QCD predictions obtained by using GRV or AFG photon PDFs and CTEQ5M proton PDFs (see Fig. 2 caption for further details).

H1 inclusive jet photoproduction

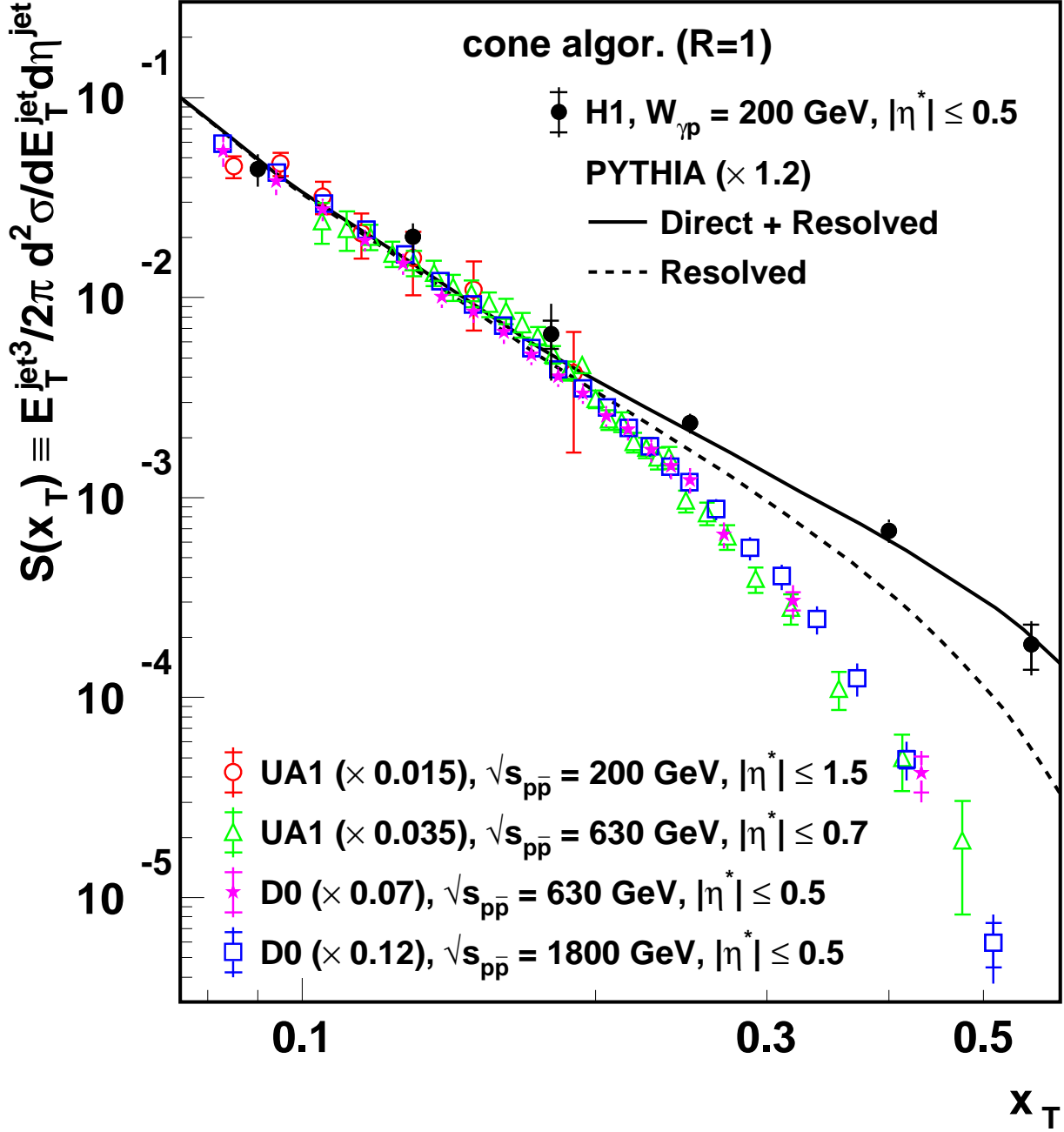


Figure 9: Scaled γp cross section at $W_{\gamma p} = 200 \text{ GeV}$ for inclusive jet production as a function of x_T for $|\eta^*| \leq 0.5$. Jets are found with the cone algorithm ($R = 1$). The data are compared with measurements from UA1 [4, 5] and D0 [6, 7] of inclusive jet production in $p\bar{p}$ collisions at various cms energies. The predictions of PYTHIA for γp and for the resolved photon contribution are also shown, multiplied by a factor 1.2 to match the normalisation of the data.